A Layered Sodium Titanate as Promising Anode Material for Sodium Ion Batteries

ARCHIVES
MASSACHUSETTS INSTITUTE OF TECHNOLOGY
MAY 2 3 2014
LIBRARIES

by

DI WU

B.S. Materials Science and Engineering
Tsinghua University (2012)

Submitted to the Department of Mechanical Engineering
in Partial Fulfillment of the Requirements for the Degree of

MASTER OF SCIENCE

at the

MASSACHUSETTS INSTITUTE OF TECHNOLOGY

June 2014

© 2014 Massachusetts Institute of Technology. All rights reserved.

Signature redacted

Signature of Author .....
Department of Mechanical Engineering
May 9, 2014

Signature redacted

Certified by .....
Gerbrand Ceder
R. P. Simmons Professor of Materials Science and Engineering
Thesis Supervisor

Signature redacted

Certified by .....
Yang Shao-Horn
Gail E. Kendall Professor of Mechanical Engineering
Thesis Reader, Co-advisor

Signature redacted

Accepted by .....
David E. Hardt
Professor of Mechanical Engineering
Chair, Departmental Committee on Graduate Students

[This page is intended to be blank.]

A Layered Sodium Titanate as Promising Anode Material for Sodium Ion Batteries

by

DI WU

Submitted to the Department of Mechanical Engineering
on May 9,2014 in Partial Fulfillment of the Requirements for the Degree of
Master of Science

Abstract

Sodium ion batteries have recently received great attention for large-scale energy applications because of the abundance and low cost of sodium source. Although some cathode materials with desirable electrochemical properties have been proposed, it's quite challenging to develop suitable anode materials with high energy density and good cyclability for sodium ion batteries. Herein, we report a layered material, O3-$NaTiO_2$, that delivers 130mAhg^{-1} of reversible capacity and presents excellent cyclability with capacity retention over 97.5% after 40cycles and high rate capability. Furthermore, by coupling the electrochemical process with *in situ* X-ray diffraction, the structure evolution and variation of cell parameters corresponding to an O3-O3' phase transition during sodium deintercalation is investigated. Unusual lattice parameter variation was observed by *in situ* XRD, which can be related to the structure modulation with varying Na vacancy ordering. An irreversible structural modification upon overcharging is also confirmed by *in situ* XRD. In summary, our work demonstrates that O3-$NaTiO_2$ is a very promising anode material for sodium ion batteries with high energy density.

Thesis Supervisor: Gerbrand Ceder
Title: R.P. Simmons Professor of Materials Science and Engineering
Thesis Reader and Co-advisor: Yang Shao-Horn
Titile: Gail E. Kendall Professor of Mechanical Engineering

[This page is intended to be blank.]

Acknowledgement

First and sincerely, I would like to thank my supervisor Professor Gerbrand Ceder for offering me the great opportunity to do exciting scientific research in his group and for his great inspiration and motivation through my master's study. With profound scientific knowledge and insightful vision of energy storage material, Prof. Ceder has guided the whole group to great science. His dedication to science and his enthusiasm on research will always inspire me in my future career.

I would like to specially thank Prof. Yang Shao-Horn for her valuable time and thoughtful advices for my thesis.

I would also like to thank Dr. Xin Li, Dr. Lei Liu, Dr. Bo Xu and Prof. Hailong Chen for their guidance, generous supports and fruitful collaborations.

Every former and present member of Ceder group is sincerely acknowledged. My heartly gratitude goes to Nancy Twu for all the experimental trainings and friendly help. I'm very grateful for all the experimentalists, Xiaohua Ma, Jae Chul Kim, Rui Wang, Jinhyuk Lee, Yuechuan Lei, Ian Matts and Plousia Vassilaras. You shared your expertise with me and make the time working in the lab delightful. I would also like to thank all the computationalists, Piero Canepa, Eric Wang, Hong Zhu, Dong-Hwa Seo, Sai J, Sai G, Rahul Malik, Edmanuel Torres, Alex Urban, Alex Toumar, Aziz Abdellahi, Steve Dacek, Wenxuan Huang, ShinYoung Kang, Daniil Kitchaev, Will Richards, Ziqin Rong, Wenhao Sun, and Lusann Yang. I learned a lot from everyone both scientifically and personally. Also I would like to thank Kathryn Simons for her kindly help and friendly smile all the time.

I must express my gratitude to my friends at MIT, especially for my dearest roommates Qifang Bao and Yi Huang who share all the delights and sorrows with me. I couldn't thank

my friend Dong Guan enough for his great support during my darkest days in life. Also I would like to thank my friends Xinchen Ni, Ling Ren, Qianru Wang, Wenzhen Yuan, Lei Zhou, Tianshi Fang, Mo Chen, and Duanhui Li for making my life at MIT more involved and colorful. I feel so lucky to be friends with all of you.

My deepest gratitude goes to my beloved mom. You are always my source of strength and courage. Without your support, I would never be where I am today. I owe you a thousand apologies. Although I cannot see you anymore, I could feel your love always surrounding me. And I'm always missing you and loving you, deep in my heart, deep in my soul.

Table of Contents

List of Figure Captions 9

CHAPTER 1. Introduction and motivation of the thesis 13

1 Introduction and motivation 13

CHAPTER 2. Experimental Study of O3-type $NaTiO_2$ 16

2.1 Materials and methods 16

2.1.1 Solid-state synthesis of O3 $NaTiO_2$ 16

2.1.2 Structure characterization by X-ray diffraction 16

2.1.3 Electrochemical tests 17

2.1.4 *In situ* X-ray diffraction 17

2.2 Results and Discussions 18

2.2.1 Structure of O3 $NaTiO_2$ 18

2.2.2 Electrochemical performances 19

2.2.2.1 Open-circuit-voltage (OCV) test 19

2.2.2.2 Galvanostatic charge and discharge of $NaTiO_2$ 22

2.2.2.3 Optimization of capacity and cyclability 26

2.2.2.4 Rate capability 35

2.2.2.5 Potentionstatic intermittent titration test (PITT) results 37

CHAPTER 3. Understanding of mechanism **41**

3.1 Structure evolution study by *in situ* XRD 41

3.2 Irreversible structure modification upon overcharge 54

CHAPTER 4. Conclusions **57**

Reference 58

List of Figure Captions

Figure 2.1.	XRD pattern of O3-type $NaTiO_2$ synthesized by solid-state reaction.	18
Figure 2-2.	OCV profiles of $NaTiO_2$ powder with dehydrated electrolyte and as-prepared electrolytes tested in Swagelok cells for 24 hours.	21
Figure 2-3.	OCV profiles of $NaTiO_2$ powder, $NaTiO_2$ film bind by PTFE, NaTiO2 and carbon mixture film bind by PTFE, tested in Swagelok cells for 24 hours.	21
Figure 2-4.	Voltage versus capacity profile of $NaTiO_2$ galvanostatic charged/discharged at C/10 rate for 10 cycles in the voltage range of 0.6-1.6V.	23
Figure 2-5.	Voltage versus capacity profile of $NaTiO_2$ galvanostatic charged/discharged at C/10 rate for 10 cycles in the voltage range of 0.8-1.6V.	24
Figure 2-6.	Voltage versus Na content per formula unit galvanostatic charged/discharged at C/10 rate for 10 cycles in the voltage range of 0.6-1.6V.	25
Figure 2-7.	Voltage versus capacity profile of $NaTiO_2$ galvanostatic charged/discharged at C/10 rate for 10 cycles in the voltage range of 0.7-1.6V.	27
Figure 2-8.	Comparison of voltage profiles versus sodium content with different cutoff voltage 0.6V, 0.7V and 0.8V.	28
Figure 2-9.	Voltage versus capacity profile of $NaTiO_2$ galvanostatic charged/discharged at C/10 rate for 10 cycles in the voltage range of 0.5-1.6V.	29
Figure 2-10.	Capacity versus cycle index of $NaTiO_2$ galvanostatic charge/discharge at C/10 with different low cutoff of voltage	30
Figure 2-11.	Voltage versus capacity profile of $NaTiO_2$ galvanostatic charged/discharged at C/10 rate for 10 cycles in the voltage range of 0.6-1.7V.	31
Figure 2-12.	Voltage versus capacity profile of $NaTiO_2$ galvanostatic charged/discharged at C/10 rate for 10 cycles in the voltage range of 0.6-2.0V.	32
Figure 2-13.	Comparison of voltage curve with different high cutoff voltage	33

Figure 2-14.	Capacity versus cycle index of $NaTiO_2$ galvanostatic charge/discharge at C/10 with different high cutoff of voltages	33
Figure 2-15.	Cyclability of $NaTiO_2$ at C/10 in 0.6-1.6V voltage window	34
Figure 2-16.	Capacity versus cycle index of $NaTiO_2$ galvanostatic charge/discharge at C/10 rate with different low cutoff voltage	34
Figure 2-17.	Rate capability of $NaTiO_2$	36
Figure 2-18.	Capacity versus voltage of Na deintercalation and intercalation for $NaTiO_2$ measured by PITT in the 0.6-1.6V voltage window	38
Figure 2-19.	Capacity versus voltage of Na deintercalation and intercalation for NaTiO2 measured by PITT in the 0.6-1.7V voltage window	39
Figure 3-1.	X-ray diffraction patterns in the 6.5o-30.5o two-theta range (Kα1&Kα2 of Mo source) of an *in situ* cell continuously charged/discharged at C/20 rate	42
Figure 3-2.	Schematic illustration of O3 structure and simulated XRD pattern	43
Figure 3-3.	Evolution of $(003)_{hex}$ peak from *in situ* XRD during galvanostatic charge at C/20.	44
Figure 3-4.	Lattice parameters a_{hex} and c_{hex} of O3 phase calculated from *in situ* XRD upon charge	44
Figure 3-5.	Schematic illustration of O3' structure and simulated XRD pattern.	45
Figure 3-6.	Evolution of $(104)_{hex}$ peak from *in situ* XRD during galvanostatic charge and discharge at C/20 rate.	46
Figure 3-7.	Evolution of peaks in the 12°-17° two-theta range from *in situ* XRD during during galvanostatic charge and discharge at C/20 rate.	47
Figure 3-8.	Variation of intersheet $(001)_{mon}$ and intrasheet $(010)_{mon}$ distance versus sodium content of O3' phase from *in situ* XRD during charge.	49
Figure 3-9.	Variation of intersheet $(001)_{mon}$ and intrasheet $(100)_{mon}$ distance versus sodium content of O3' phase from *in situ* XRD during charge.	49
Figure 3-10.	Variation of a_{mon}, b_{mon}, c_{mon} and β_{mon} versus sodium content of O3' phase from *in situ* XRD during charge.	50
Figure 3-11.	*In situ* XRD data in the 10°-20° two-theta range recorded	51

during the PITT experiments.

Figure 3-12. (a) Evolution of $(001)_{mon}$ peak from *in situ* XRD during PITT test; (b) Evolution of $(111)_{mon}$ and $(20\text{-}2)_{mon}$ peaks from *in situ* XRD during PITT test. 51

Figure 3-13. Synergy between lattice parameter variation and superstructure evolution 52

Figure 3-14. Overall evolution of the lattice parameters a_{hex} and c_{hex} calculated from *in situ* XRD during charge. 52

Figure 3-15. In situ XRD patterns during charge from 1.6V up to 1.87V. 53

1 Introduction and motivation

Sodium-ion batteries have been attracting increasing attention for large-scale energy storage applications due to the natural abundance and low cost of sodium resources[1]. Compared with Li, although their physical and chemical properties are similar, Na has larger ionic radius (0.97Å) and higher redox potential (-2.71V vs. SHE)[1-3]. Moreover, the interactions between Na ions and the host crystal structures may be different with the Li analogues. Na intercalation/deintercalation mechanism has not been well investigated[1-4]. So there may be opportunities to develop novel electrode materials for Na-ion batteries of comparable energy density with Li-ion batteries.

The most commonly applied anode material in Li-ion batteries is graphite. Graphite delivers a moderate Li storage capacity of approximately 350mAhg^{-1} at 0.1V vs. Li^+/Li[1,5,6]. However, Na cannot be inserted into the graphite layer related to thermodynamics issues[5]. Currently, only a few materials have been reported as applicable anode for Na-ion batteries[1,3,4,6-9]. Thus, designing an anode material with large reversible capacity, moderate storage voltage, and good cyclability is critical for the development of Na-ion batteries.

Among the available anode materials for Na-ion batteries, hard carbon exhibits reversible capacity of 250mAhg^{-1} with stable cycle performance in $NaClO_4$/EC:DEC electrolyte[6]. But the average sodium storage voltage in hard carbon is relatively low (~0.1V). Most of the usable capacity is located near the sodium plating voltage, which causing potential safety concerns. Several alloys such as Sn and Sb have

shown very high storage capacity(~600mAhg^{-1})[9,8]. However, owing to the undesired large volume change during sodium insertion and extraction, the use of optimized binders and electrolyte additives is required to achieve satisfactory cyclability[3,8,9]. Oxides are also explored as potential candidates for negative electrodes of Na-ion batteries. One of the potential anodes attracting much attention is $Na_2Ti_3O_7$, which delivers over 200mAhg^{-1} initial capacity. There are basically two issues with this material. 1). The average storage voltage is 0.2V that may cause the risk of sodium plating; 2) The cycling performance is not satisfied. Recently, the spinel $Li_4Ti_5O_{12}$ was demonstrated by Y. Sun as a potential negative electrode material[7]. $Li_4Ti_5O_{12}$ deliver a reversible capacity of 155 mAhg^{-1} with good cyclability in Na-ion battery when particularly using carboxymethyl-cellulose sodium as the binder. A new anode material with excellent cyclability, P2-$Na_{0.66}[Li_{0.22}Ti_{0.78}]O_2$, was reported by the same group[4,10]. P2-$Na_{0.66}[Li_{0.22}Ti_{0.78}]O_2$ exhibits a reversible capacity of 116mAhg^{-1} at an average storage of 0.75V. The most interesting property of this P2-type material is the negligible volume change (0.77%) during sodium insertion and extraction. However, these two sodium titantes still haven't reached the goal for anode materials of high energy density and low cost. $Li_4Ti_5O_{12}$ faces the problem of high demand and increasing price of Li resource, while the usable capacity of P2-$Na_{0.66}[Li_{0.22}Ti_{0.78}]O_2$ is limited to 100mAhg^{-1} corresponding to 1/3 Na per formula unit. Therefore, developing new anode materials with high energy density still requires much investigation.

One possible type of candidate that could satisfy the high energy density standard is layered material. Research on layered $NaMO_2$(M=3d transition metal, such as Mn,

Fe, Co, Ni, V) as intercalation materials began in the 1980s[11-14]. They are drawing more attention since 2010s as promising cathode materials for sodium-ion batteries[4,15-24]. Layered Na_xMO_2 possesses different crystal structures. By the notation defined by Delmas et al.[12], On(n=1,2,3,etc) represents structures in which Na is octahedrally coordinated with oxygen, and n refers to the repeat period of the transition metal stacking. Pn(n=1,2,3, etc) represents structures where Na atoms occupy trigonal prismatic sites. Among the 3d transition metals, Ti compounds exhibit a lower redox potential compared with Mn, Fe, Co, Ni compounds[1,11,13,14,16]. So O3-$NaTiO_2$ can be a potential candidate for negative electrode. In the 1980s, Mazzaz et al. examined the electrochemical performance of O3-$NaTiO_2$[11]. However, only 0.3 Na (corresponding to 78 $mAhg^{-1}$) was reported to be reversible cycled in this O3-type material. Monoclinic $NaMnO_2$ and $NaNiO_2$ were revisited as positive electrode materials recently by Ceder group[17,18]. Their results showed that, in contrast to previous report[17], monoclinic $NaMnO_2$ can reversibly intercalate/deintercalate about 0.8 Na and $NaNiO_2$ can reversibly intercalate/deintercalate about 0.5 Na. The larger reversible capacity compared with the reports back in 1980s may result from the improvement of electrolytes.

Hence, in this thesis, the electrochemical performance of O3-$NaTiO_2$ is re-investigated, aiming at developing an anode material for sodium-ion batteries with high energy density. In addition, sodium insertion mechanism is studied by in situ X-ray diffraction during electrochemical cycling of batteries.

2 Experimental Study of O3-type $NaTiO_2$

2.1 Experimental methods

2.1.1 Solid-state synthesis of $NaTiO_2$

O3-type $NaTiO_2$ is synthesized by a solid-state reaction. TiO_2 anatase(Sigma Aldrich, 99.99%) and freshly cut Na(Sigma Aldrich) with 5% excess were placed in a Swagelok-type stainless steel tube, which was sealed in an argon-filled glove box. The tube was then fired at 920°C for 12 hours in a flow of argon gas[11,25]. After cooling, the tube was opened by tube cutter in the glove box to prevent exposure to air and moisture since $NaTiO_2$ is highly reductive.

2.1.2 Structure characterization by X-ray diffraction

The X-ray diffraction (XRD) patterns were collected on a Rigaku RU300 rotating anode diffractometer equipped with Cu Kα1 radiation in the 2θ range of 10°-85°. All the samples were sealed with Kapton film to avoid air exposure. Rietveld refinement and profile matching of the powder diffraction data of the as-prepared $NaTiO_2$ were performed using PANalytical X'Pert High Score Plus.

2.1.3 Electrochemical tests

Active material $NaTiO_2$ and conductive agent carbon black (Timcal, Super P) were manually mixed with agate mortar and pestle for 30 minutes. The mixture was then mixed with polyethylenetetrafluoride (PTFE) (Dupont, Teflon 8C) binder in a weight ratio of 85:15:5 and rolled into a thin film. The 1M NaPF6 in EC: DEC electrolyte was

prepared by dissolving anhydrous NaPF6 (98%, Sigma Aldrich) into ethylene carbonate: diethylcarbonate (EC: DEC) solution (anhydrous Sigma Aldrich, 1:1 in volume ratio). Na metal film was used as counter electrode. Two pieces of glass fiber served as separators and stainless steel as current collectors in customized Swagelok cells, assembled in an argon-filled glove box with the oxygen and moisture levels less than 0.1ppm. Cells were tested on a Maccor 2200 or Arbin BT2000 operating at room temperature. The loading density of the active material was kept to be approximately $3mg/cm^2$. A 1C rate was estimated based on 260.5 $mAhg^{-1}$. Potentiostatic intermittent titration test (PITT) was performed on a Solartron 1470E electrochemical potentiostat. Steps of 10mV were taken to fully charge and discharge the cell. The capacity was measured at each voltage step until the relax time was longer than 3 hours or 10hours.

2.1.4 *In situ* X-ray diffraction

In situ X-ray diffraction experiments during electrochemical cycling of batteries were collected on a Bruker D8 Advance Da Vinci Mo-source diffractometer with step scans between 6.5^{o}-30.5^{o} 2θ. An *in situ* battery was designed with a Be window for X-ray penetration. The battery was configured with $NaTiO_2$ electrode as the working electrode, sodium as the counter electrode, 1M NaPF6/EC:DEC as the electrolyte and glass fiber as the separator. The charge/discharge of *in situ* battery was carried on a Solartron electrochemical potensiostat in the voltage range of 0.6-1.6V at a current rate of C/20, or at each relaxation step of PITT test charge with steps of 30mV and step duration of 4 hours.

2.2 Results and Discussions

2.2.1 Structure of O3-type $NaTiO_2$

The X-ray diffraction pattern of as-prepared O3-type $NaTiO_2$ is shown in Fig 2-1. A pure O3-type $NaTiO_2$ phase was obtained by solid-state method. The background and three broad peaks between 10°-30° are from the Kapton film. The profile is fitted to the structure referenced in ICSD (#43439) with the space group R-3m. Rietveld refinement gives the lattice parameters a=3.032Å, b=3.032Å, c=16.325Å. These values are in good agreement with cell parameters previously reported[11,25].

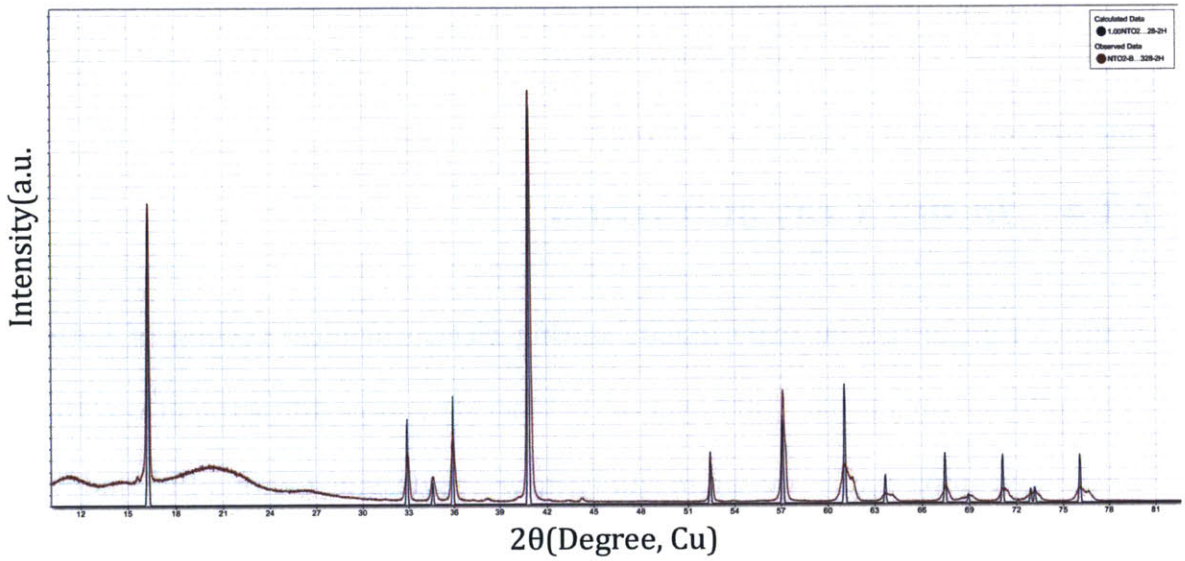

Figure 2-1 XRD pattern of O3-type $NaTiO_2$ synthesized by solid-state reaction.

Since $NaTiO_2$ is insoluble in concentrated nitric acid, aqua regia, and aqueous hydro fluoride (HF)[25], chemical analysis such as inductively coupled plasma atomic emission spectroscopy(ICP-AES) could not be performed.

In addition, $NaTiO_2$ is very air-sensitive due to the very strong reducing property of Ti^{3+} ion. Even very short-term exposure in air results in oxidation by oxygen and hydrolysis reaction with water, which will destroy the original structure of $NaTiO_2$. So currently morphology characterization by scanning electron microscopy (SEM) cannot be performed since special sample holder that keeps the sample in vacuum before transferred to and evacuated in SEM is required.

2.2.2 Electrochemical performance

2.2.2.1 Open-circuit-voltage (OCV) test

$NaTiO_2$ is extremely sensitive to moisture level. Even trace amount of water in the battery system, especially in the electrolyte, will cause desodiation of $NaTiO_2$ by hydrolysis. Since cell open circuit voltage is a function of sodium content, an increase of open circuit voltage will instantly reflect the extent of desodiation.

Before cell assembly, every component of the Swagelok-type cell, including PTFE body and caps, stainless steel current collectors and glass fiber separators, are dried overnight in an oven at 80°C in order to remove water absorbs on the surfaces. Thus trace amount of water in the battery system mainly comes from the electrolyte. Therefore, it's crucial to desiccate the organic electrolyte.

Molecular sieve is a porous material with small holes to block large molecules while allowing small molecules to pass[26]. Many molecular sieves are used as desiccants. So molecular sieves are added to the as-made NaPF6-EC:DEC(1:1) electrolyte and rotated to remove the trace water. Karl Fischer titrations were performed to

evaluate the water content in electrolytes[26]. The results indicated that less than 1ppm of water was present in the dehydrated electrolyte, which is the limit of detection of the device, compared with about 5ppm of water in the as-made electrolyte.

Open-circuit-voltage tests of as-prepared $NaTiO_2$ powder were performed on both Swagelok-type cells assembled with dehydrated electrolyte and as-made electrolyte. Since the composition and concentration of electrolytes are the same, the difference of OCV profiles is due to different amount of trace water in the electrolyte. The slope of OCV curve is a good measurement of the rate of desodiation reaction. When the slope is larger, desodiation reaction is faster, which indicates that the amount of trace water in the electrolyte is larger.

OCV profiles of $NaTiO_2$ powder versus Na metal counter electrode (Na^+/Na) tested in Swagelok-type cells for 24 hours are shown in Fig2-2. At the beginning, OCV of $NaTiO_2$ with dehydrated electrolyte can be as low as 0.642V, while OCV of that with as-made electrolyte is 0.69V. The slope of OCV of $NaTiO_2$ powder with as-made electrolyte is about 0.005V/h. While the slope of OCV curve of $NaTiO_2$ powder with dehydrated electrolyte is not only much smaller, but also quickly converges to a stable value. This indicates a very low level of trace water in the dehydrated electrolyte. These results demonstrate that 1) $NaTiO_2$ is a sensitive and visualized indicator of the amount of trace water in the electrolyte; 2) Molecular sieves can effectively dehydrate organic electrolyte; 3) After dehydration treatment, it's reasonable to assume that the amount of residual water in the electrolyte is negligible.

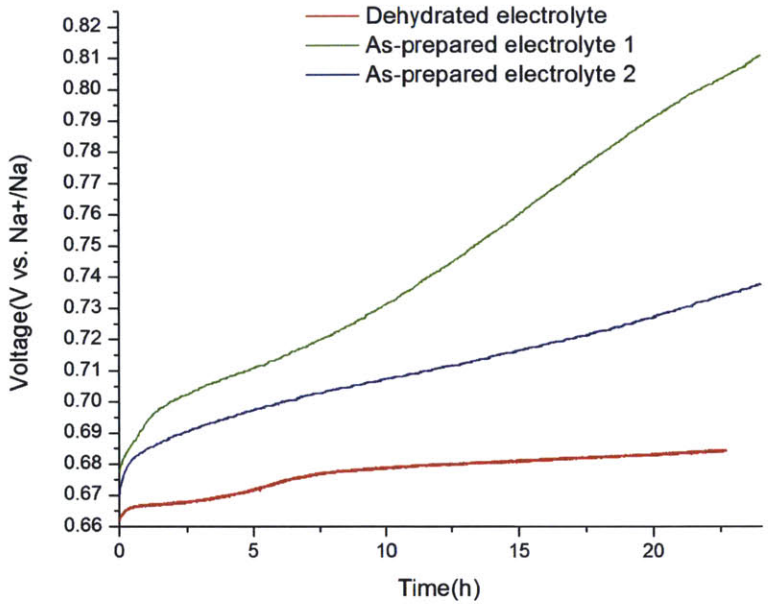

Figure2-2. OCV profiles of $NaTiO_2$ powder with dehydrated electrolyte and as-prepared electrolytes tested in Swagelok cells for 24 hours.

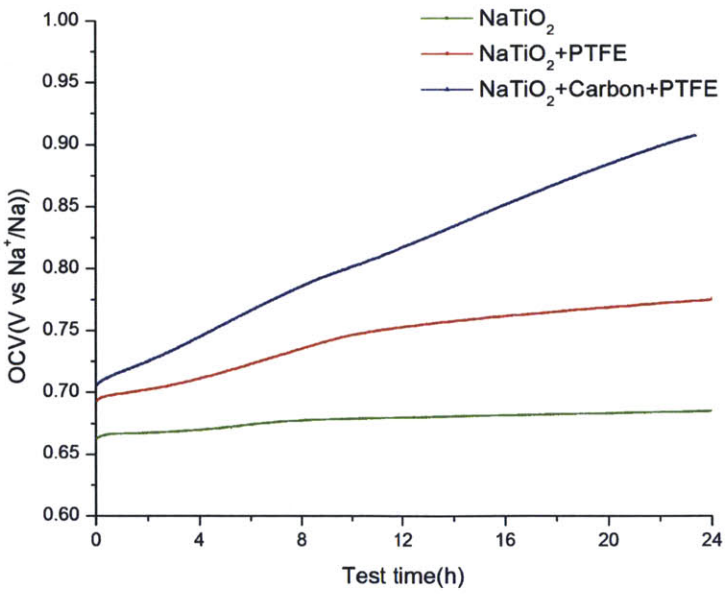

Figure2-3. OCV profiles of $NaTiO_2$ powder, $NaTiO_2$ film bind by PTFE, $NaTiO_2$ and carbon mixture film bind by PTFE, tested in Swagelok cells for 24 hours.

OCV profiles of $NaTiO_2$ powder, $NaTiO_2$ film bind by PTFE, $NaTiO_2$ and carbon mixture film bind by PTFE, tested in Swagelok cells for 24 hours are shown in Fig2-3. At the beginning, the OCV values of fresh batteries are 0.662V, 0.674V and 0.693V respectively. When $NaTiO_2$ is mixed with PTFE, the rate of sodium loss is faster than that of pure $NaTiO_2$ powder, possibly due to reaction between $NaTiO_2$ and PTFE. Desodiation reaction is a Faradic reaction that accompanied with charge transfer. After mixed with carbon, electronic conductivity of electrode film is improved and thus desodiation reaction rate is faster. This explains the steeper slope of OCV curve of $NaTiO_2$ and carbon mixture film bind by PTFE. Meanwhile, carbon black and PTFE also contain certain amount of trace water even after drying at high temperature, which is another possible reason of the higher desodiation rate. Additionally, porous carbon can irreversibly insert Na ions, which is also a possible cause of the faster desodiation behavior.

From the above results, it's clear that the OCV of O3-type $NaTiO_2$ is about 0.64V, which is much lower than the previous report value of 0.8V[11]. The previous study of $NaTiO_2$ neglected the specific capacity below 0.8V. Our study demonstrates that the specific capacity below 0.8V can be reversibly cycled, which will be discussed in 2.2.2.2.

2.2.2.2 Galvanostatic charge and discharge of $NaTiO_2$

Fig2-4 shows the voltage profiles during galvanostatic charge and discharge of $NaTiO_2$ at C/10 rate for 10cycles (1C=260.5mAhg^{-1}). At first, the battery is discharged to 0.6V to compensate Na loss and thus obtain fully discharge state. O3-

$NaTiO_2$ delivers 134.5mAhg^{-1} of reversible capacity in the voltage range of 0.6-1.6V, which corresponds to approximately 52% of the theoretical capacity, or 0.52Na insertion/extraction per formula unit, based on a single-electron redox process of Ti^{3+} /Ti^{4+} couple. In the 0.6-1.6V range, the very strong similarity between the discharge and charge curves clearly shows that the intercalation/deintercalation process is reversible with a small polarization.

In the voltage range of 0.8-1.6V, the specific capacity is approximately 100 mAhg^{-1}, corresponding to 38% of the theoretical capacity. The obtained capacity is slightly larger than previous report[11]. In the low voltage range of 0.6-0.8V, O3-$NaTiO_2$ delivers a capacity of approximately 35 mAhg^{-1}, corresponding to 14% of the theoretical capacity. Moreover, the capacity in the low voltage range is truly reversible. This result is significant because reversible capacity in the low voltage range is especially crucial for anode materials.

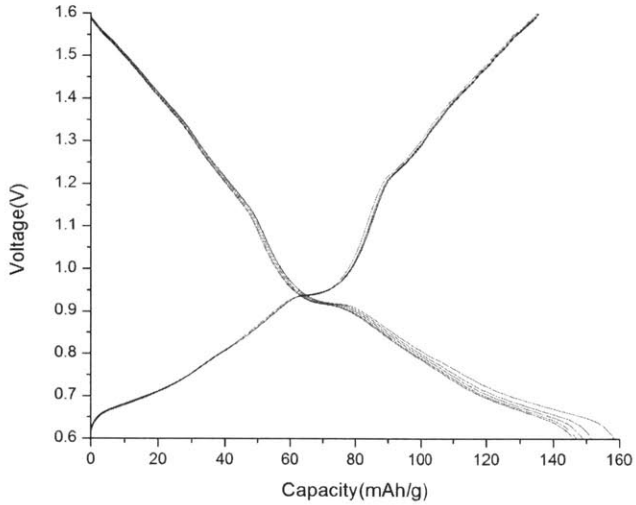

Figure2-4. Voltage versus capacity profile of $NaTiO_2$ galvanostatic charged/discharged at C/10 rate for 10 cycles in the voltage range of 0.6-1.6V.

An irreversible capacity loss was observed in the first discharge, which can be ascribed to the formation of solid electrolyte interphase layer (SEI) and sodium insertion into carbon when discharged to a low voltage. This is a common phenomenon in the negative electrodes of lithium-ion batteries[4,27].

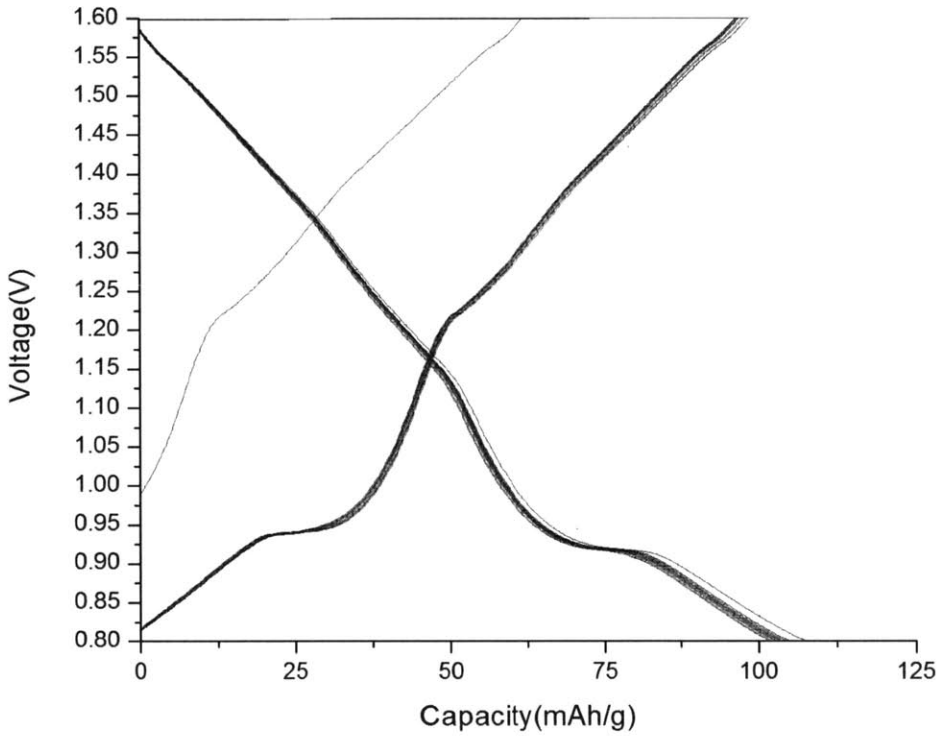

Figure2-5. Voltage versus capacity profile of $NaTiO_2$ galvanostatic charged/discharged at C/10 rate for 10 cycles in the voltage range of 0.8-1.6V.

The data in Fig2-4 can also be represented in Fig2-6 where Na content is plotted versus voltage. The battery is discharged to 0.6V to reach the fully discharged state and therefore, in the following cycle, the initial Na content is determined as 1. About

0.52 Na, corresponding to a charge capacity of 134mAhg^{-1} can be deintercalated from $NaTiO_2$ when the cell is charged up to 1.6V vs. Na+/Na. Upon discharge to 0.6V, 0.53Na, corresponding to discharge capacity 138.5 mAhg^{-1} can be intercalated back to the host structure. So the sodium insertion and extraction is reversible when the cell is cycled in the range of $0.47<x<1$ in Na_xTiO_2.

The average voltage of sodium insertion into $NaTiO_2$ is about 1V.

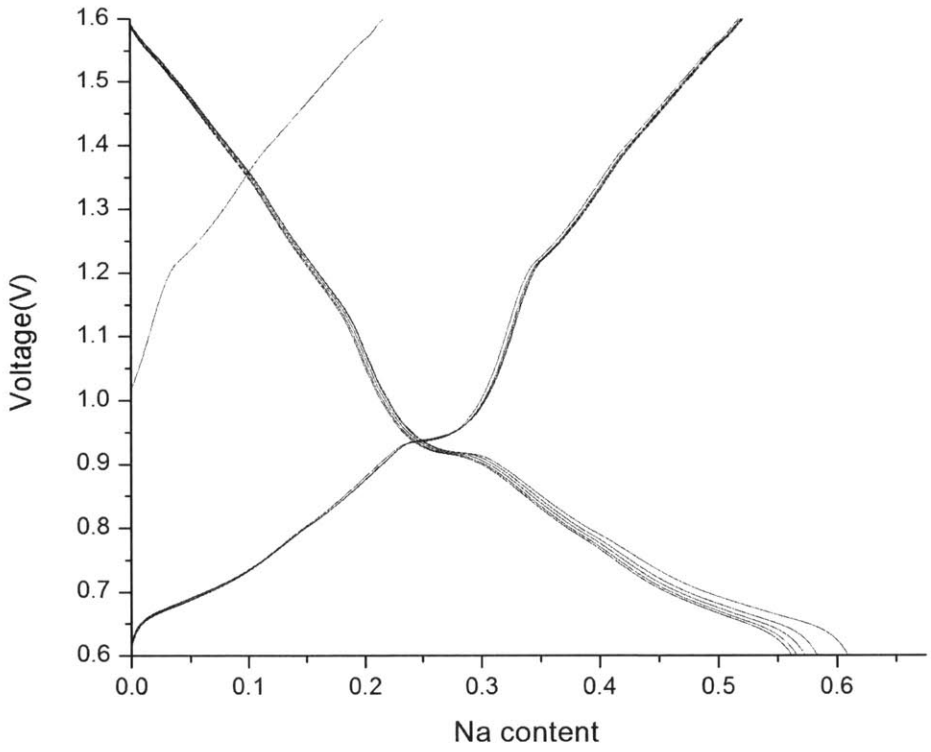

Figure2-6. Voltage versus Na content per formula unit galvanostatic charged/discharged at C/10 rate for 10 cycles in the voltage range of 0.6-1.6V.

The shape of the voltage curve exhibits a potential plateau at 0.93V, which is a characteristic of biphasic domain (corresponding to a O3-O3' phase transition), and

continuous variations of the voltage versus the composition showing the existence of solid solutions. Potential inflection in the curve at 1.20V indicates the existence of special ordering of Na+/vacancy in the interslab space of the layered structure. *In situ* X-ray diffraction studies are carried out during the electrochemical intercalation/deintercalation process to investigate the trend of structure evolution, and thus get an understanding of electrochemical reaction mechanism, which will be discussed later.

2.2.2.3 Optimization of capacity and cyclability

To obtain large capacity as well as good cyclability of $NaTiO_2$, the effect of cutoff voltage on electrochemical performance is investigated.

2.2.2.3.1 Effect of cutoff voltage in the low voltage region

Fig2-5 shows a reversible capacity of 98.7mAhg^{-1} (corresponding to 0.38 Na insertion per formula unit) when $NaTiO_2$ is cycled in the 0.8-1.6V with an excellent cyclability. The specific capacity of charge is 96.6mAhg^{-1} after 10 cycles.

Fig2-7 shows a reversible capacity of 117.2mAhg^{-1} (corresponding to 0.45 Na insertion per formula unit) when $NaTiO_2$ is cycled in the voltage range of 0.7-1.6V, which is larger than that in the 0.6-1.6V range. The cyclability is still excellent as the specific capacity retention of charge after 10 cycles is about 99.5%.

Fig2-4 shows a reversible capacity of 134.5mAhg^{-1} (corresponding to 0.52 Na insertion per formula unit) when $NaTiO_2$ is cycled in the voltage range of 0.6-1.6V,

which is larger than that in the 0.7-1.6V range. The cyclability is still excellent as the specific capacity retention of charge after 10 cycles is about 99.6%.

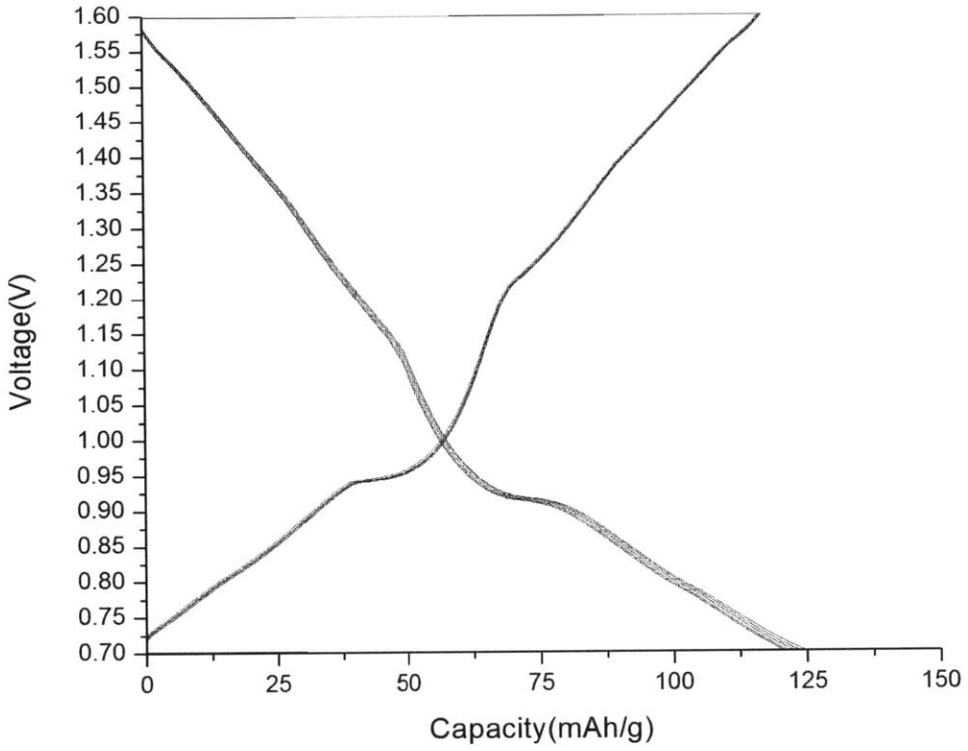

Figure2-7. Voltage versus capacity profile of $NaTiO_2$ galvanostatic charged/discharged at C/10 rate for 10 cycles in the voltage range of 0.7-1.6V.

The effect of the low cutoff voltage on the specific capacity of $NaTiO_2$ can be illustrated by a comparison of voltage profiles versus sodium content as shown in Fig2-8. As the low cutoff is decreased from 0.8V to 0.6V, larger capacity is obtained and good cyclability of the battery is maintained.

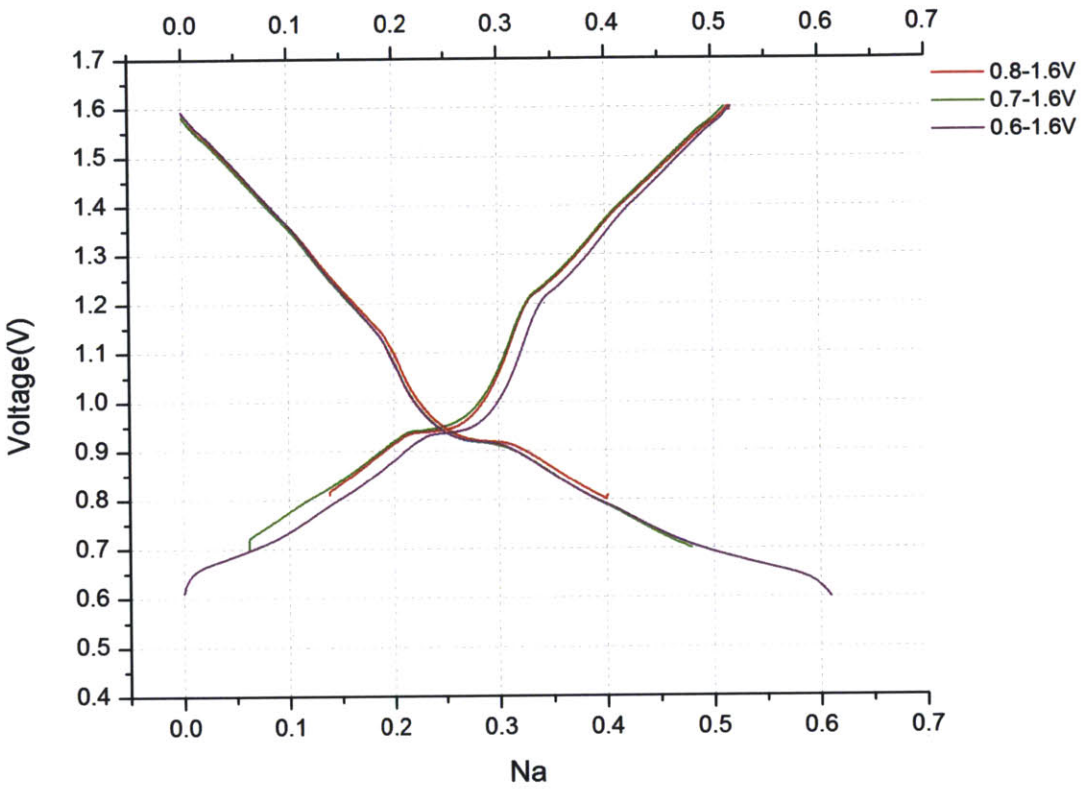

Figure2-8. Comparison of voltage profiles versus sodium content with different cutoff voltage 0.6V, 0.7V and 0.8V.

If the cutoff voltage in the low voltage region is further decreased to 0.5V, slightly larger capacity is obtained as shown in Fig2-9. For example, 135.2mAhg^{-1} and 146.7mAhg^{-1} for the 2nd charge and discharge respectively, corresponding to 0.52 Na and 0.56 Na per formula unit. For comparison, the specific capacities of the 2nd cycle of batteries cycled in the 0.6-1.6V range is 134.5mAhg^{-1} and 138.6mAhg^{-1} respectively, corresponding to 0.516 Na and 0.53 Na per formula unit. Although lower cutoff voltage slightly improves the capacities during initial cycles, it causes

deterioration of cyclability. The specific capacity is 117.9mAhg^{-1} and 123.8mAhg^{-1} for the 10th charge and discharge respectively, corresponding to 0.45 Na and 0.48 Na per formula unit. The capacity retention of charge after 10 cycles is about 88.3%, which means a faster capacity decay when the battery is cycled in the voltage range of 0.5-1.6V. The irreversible capacity loss may result from electrolyte degradation, continuous side reactions of SEI formation and irreversible sodium insertion into carbon.

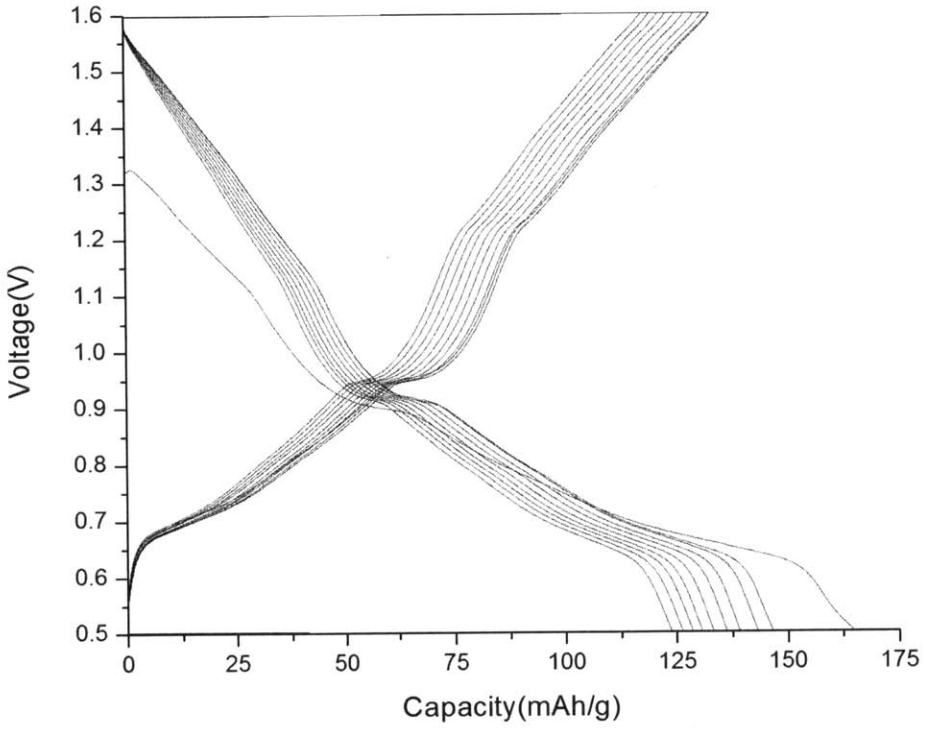

Figure2-9. Voltage versus capacity profile of $NaTiO_2$ galvanostatic charged/discharged at C/10 rate for 10 cycles in the voltage range of 0.5-1.6V.

From the shape of voltage curve in Fig2-9, it's clear to see a steep drop in the voltage curve when the battery is discharged below 0.6V. This means there is limiting electrochemical reaction of redox couples in this low voltage region. So it's not necessary to set the cut-off voltage as low as 0.5V. Therefore, choosing the cut-off voltage of 0.6V ensures $NaTiO_2$ delivers the best cyclic performance as well as large capacity.

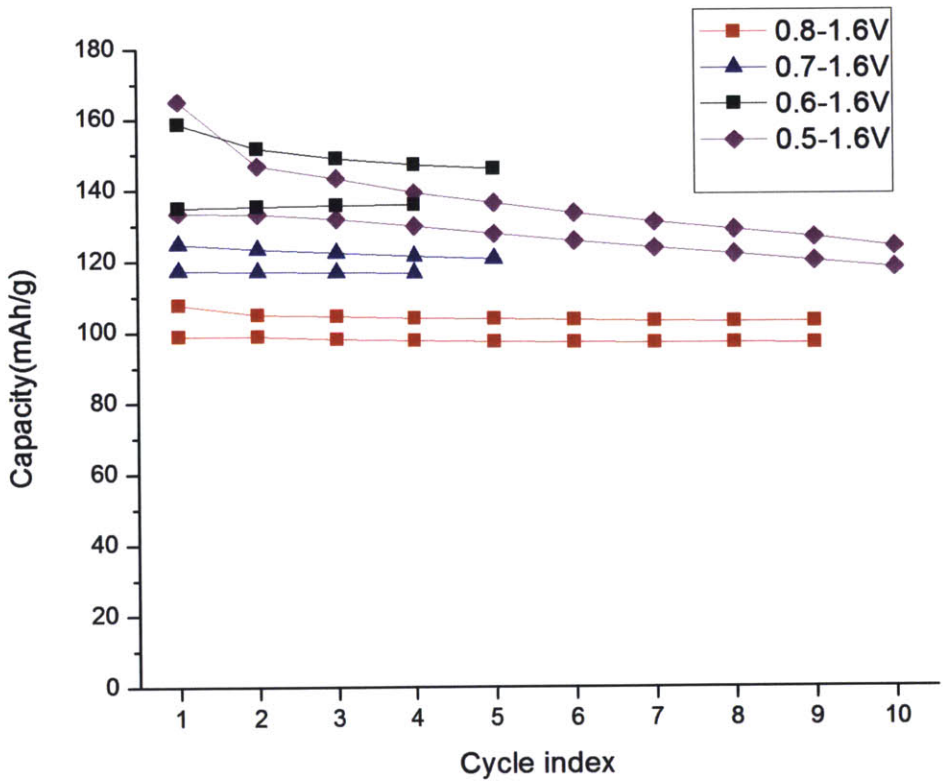

Figure2-10. Capacity vs cycle index of $NaTiO_2$ galvanostatic charge/discharge at C/10 with different low cutoff of voltage.

2.2.2.3.2 Effect of cutoff voltage in the high voltage region

From the voltage profile of battery cycled in the 0.6-1.7V range with high voltage cutoff 0.1V higher than 1.6V, obviously gradual capacity decay upon cycling is observed, as shown in Fig2-11.

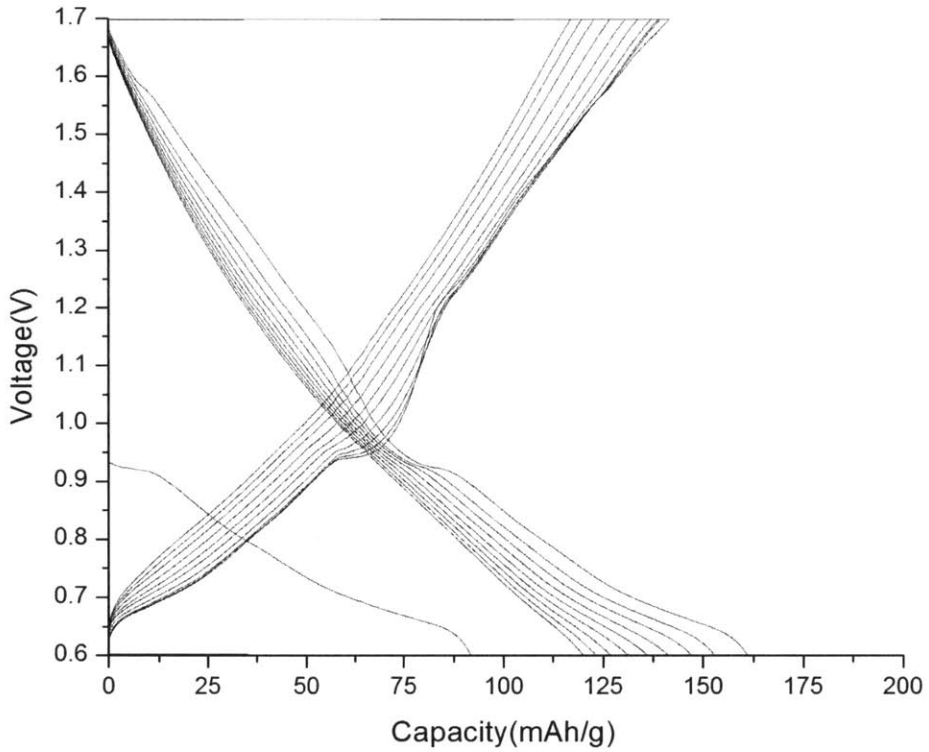

Figure2-11. Voltage versus capacity profile of $NaTiO_2$ galvanostatic charged/discharged at C/10 rate for 10 cycles in the voltage range of 0.6-1.7V.

When the battery is charged to 2V as an increased charge depth, an irreversible short voltage plateau shows up at about 1.7V, indicating an irreversible phase transition. Irreversible modifications of the material occur and the shape of the subsequent voltage versus composition discharge curve is completely changed. Previous features of voltage profile, such as voltage plateau and inflection point, disappear. This behavior is similar with previous report[11], which was explained as

irreversible migration of some Ti^{4+} ions from the transition metal layer to sodium layer. The structural evolution is confirmed by *in situ* X-ray study, which will be discussed later.

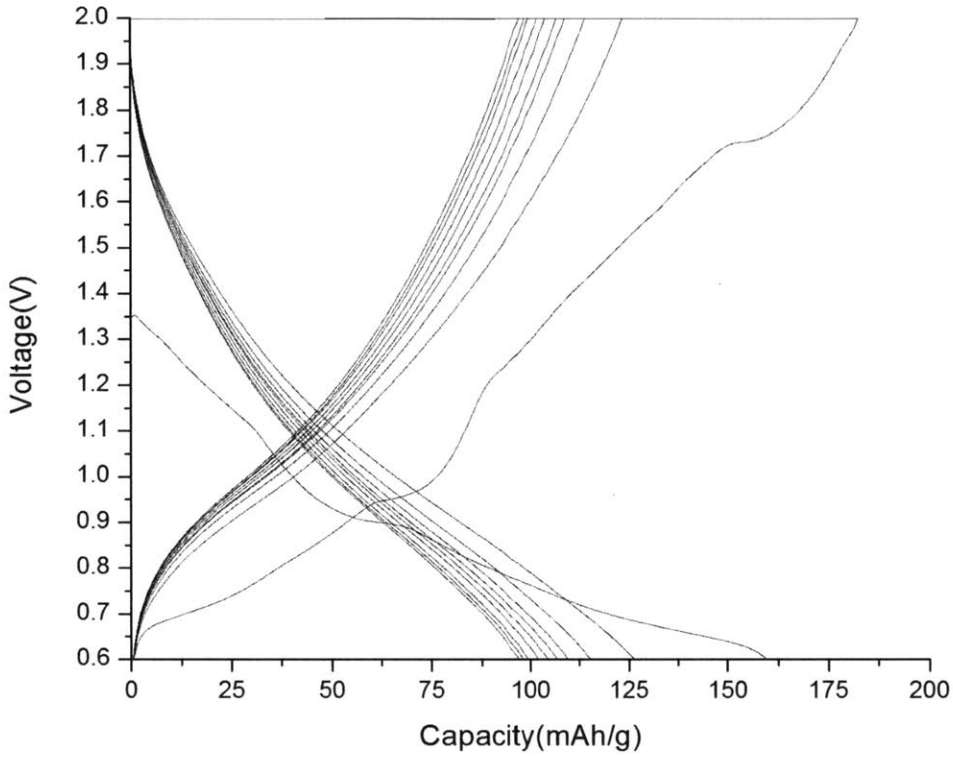

Figure2-12. Voltage versus capacity profile of $NaTiO_2$ galvanostatic charged/discharged at C/10 rate for 10 cycles in the voltage range of 0.6-2.0V.

Hence, based on the galvanostatic cycling tests, 1.6V is the optimal cutoff voltage in the high region to maintain large reversible sodium insertion and extraction and prevent irreversible structure modification in the high voltage region. A more detailed and accurate study on measuring the optimal cutoff in the high voltage region is conducted by *in situ* X-ray diffraction, which will be discussed in the next chapter.

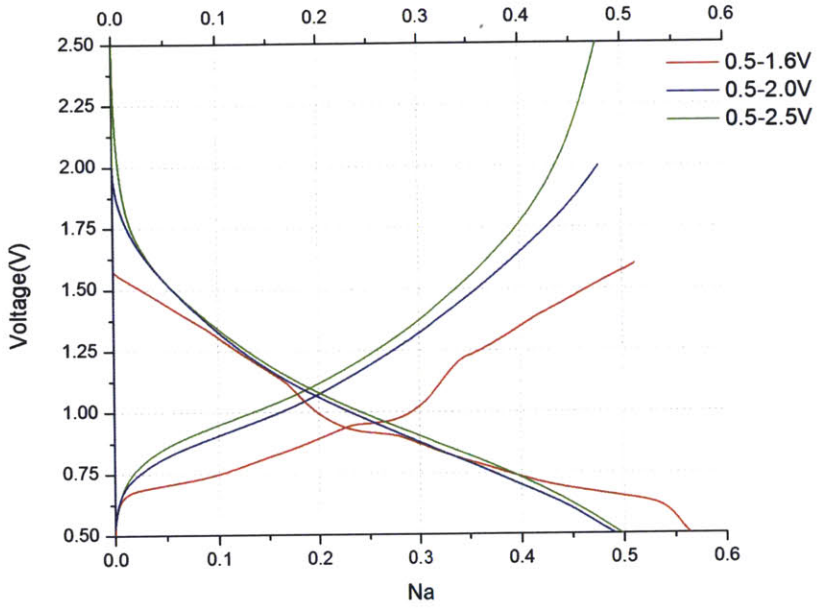

Figure2-13. Comparison of voltage curve with different high cutoff voltage

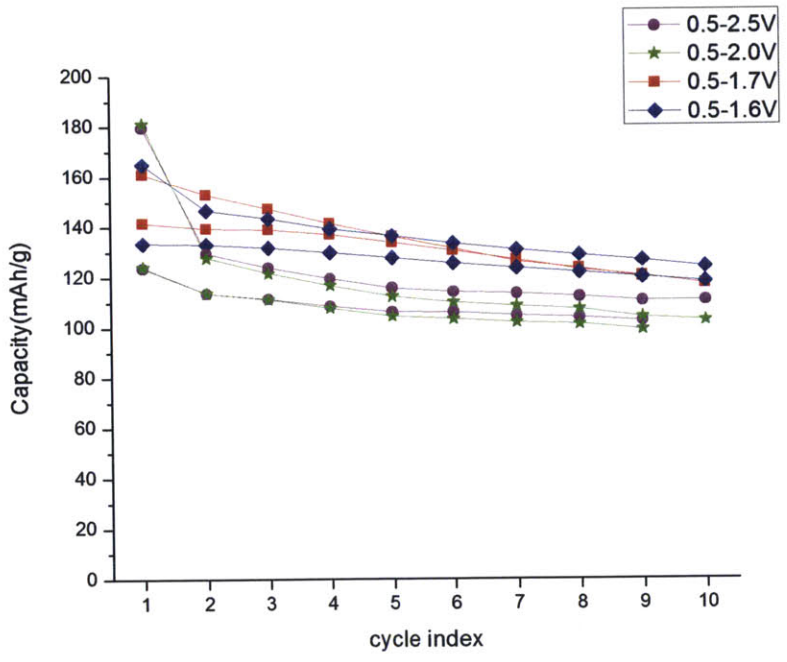

Figure2-14. Capacity vs cycle index of NaTiO2 galvanostatic charge/discharge at C/10 with different high cutoff of voltages

2.2.2.3.3 Cyclability in the optimized voltage range

Fig2-15 shows the long-term cycling performance of $NaTiO_2$ in 0.6-1.6V voltage range. The capacity retention after 40 cycles at a current rate of C/10 is about 97.3%. The relatively low Coulombic efficiency at initial cycles is possibly related to the degradation of electrolyte, formation of SEI layer or irreversible insertion of Na into carbon. O3 $NaTiO_2$ exhibits a comparable cyclability with reported negative electrode materials with long-life cyclability for sodium-ion batteries[4,7].

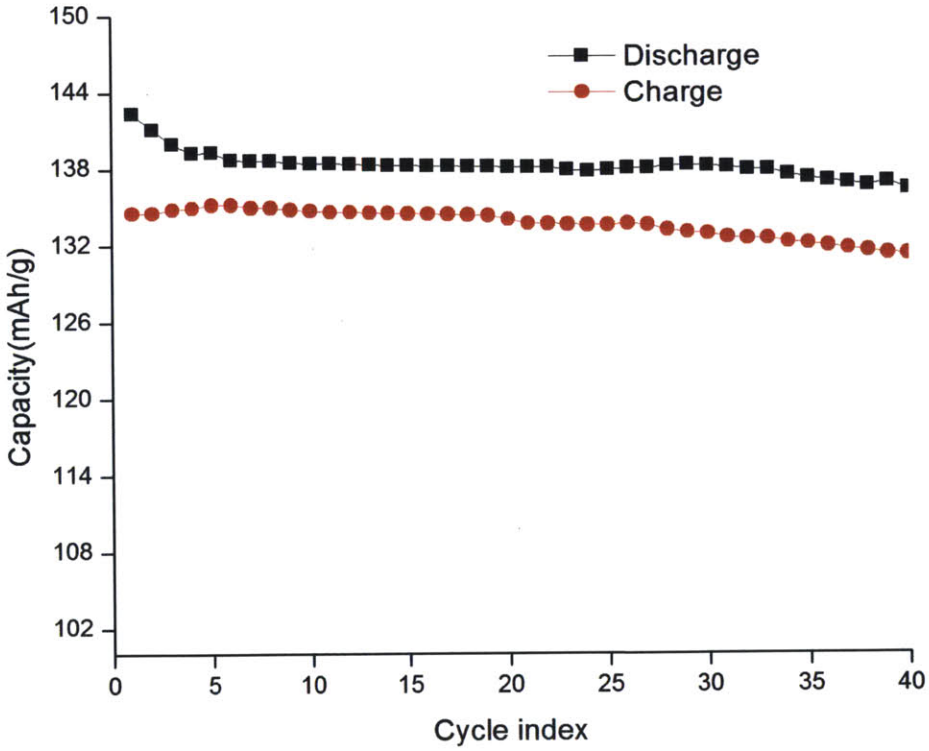

Figure2-16. Capacity vs cycle index of $NaTiO_2$ galvanostatic charge/discharge at C/10 rate for 40 cycles.

2.2.2.4 Rate capability

The rate capability of a $Na/NaTiO_2$ battery is shown in Fig2-17. The battery is discharged to 0.6V at a current rate of C/20 and then charged to 1.6V at different current rates from C/20 to 5C. It's noteworthy to emphasize that the battery still delivers large charge capacity at 1C rate, 118.7mAhg^{-1} (87.9% of C/10 rate). At C/5 rate, the battery delivers charge capacity of 135.4mAhg^{-1} (99% of C/10 rate), with small polarization. The rate capability of $NaTiO_2$ is better than some other O3-type layered materials, for example $NaMnO_2$, $NaCoO_2$ and $NaNiO_2$[14–18,22]. $NaCoO_2$ exhibits a stepwise voltage profile with limited rate capability. A possible explanation is the phase boundary movement for two-phase regions at the plateaus causes sluggish sodium diffusion[20,23]. For $NaTiO_2$, only a short plateau in the early stage of charge process as O3-O3' phase transition is observed. From our *in situ* XRD study, a biphasic domain for $NaTiO_2$ exists only at that 0.93V voltage plateau.

Note that special treatment of electrode material such as carbon coating and nanosizing is not required to obtain such good electrochemical performance. At even higher rate, for example 5C, polarization of cell voltage is considerably increased. So it's reasonable to propose that the rate capability of this material can be further optimized.

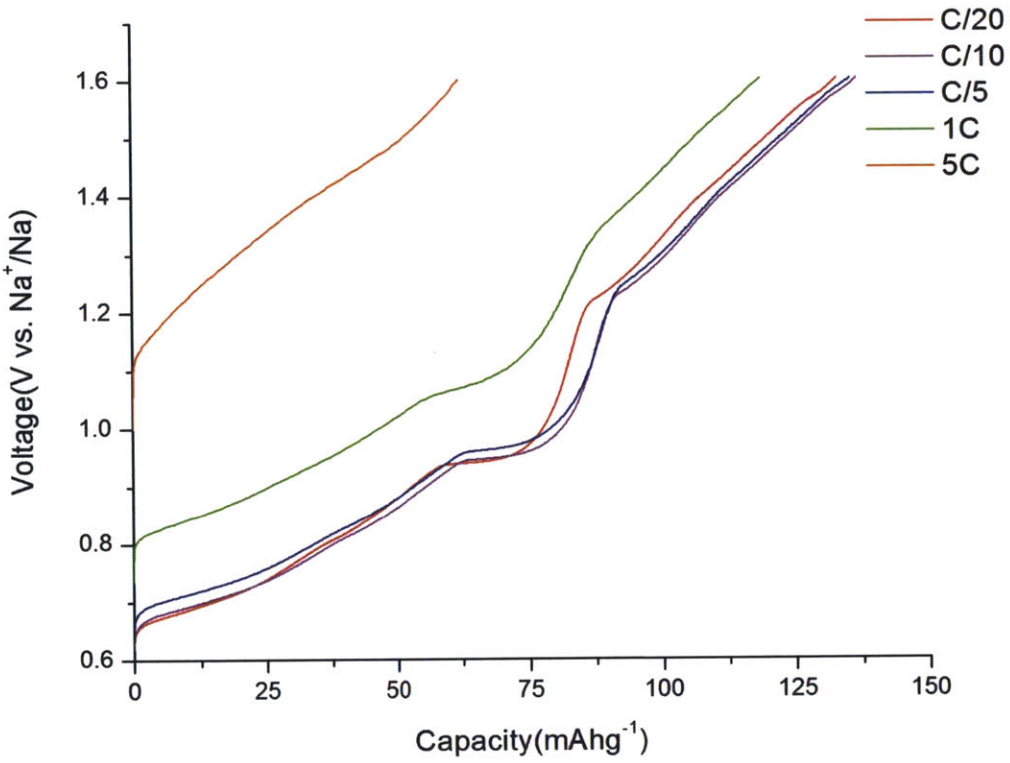

Figure2-17. Rate capability of $NaTiO_2$

Titanium is an earth-abundant element with low price. Excellent cyclability, large reversible capacity and good rate capability demonstrate that $NaTiO_2$ is by far among the best anode materials for practical application in sodium-ion batteries.

2.2.2.5 Potentionstatic intermittent titration test (PITT) results

Potentionstatic intermittent titration test (PITT) is one of the useful techniques to understand electrochemical behaviors for Li intercalation and sodium intercalation materials[16,17]. It forces diffusing ion Na^+ to get excited from its equilibrium state and records a responding current. The input of PITT is usually a small potentiostatic

voltage step of tens of millivolts. Then, electrochemically active sodium materials must react to such an input by varying its Na concentration because the Na chemical potential must correspond to the voltage. Therefore, the diffusion of Na ions must occur.

Fig2-18 shows the capacity versus voltage measured by PITT of $NaTiO_2$ in the voltage range of 0.6-1.6V. For this PITT test, the capacity was measured at each voltage step until the current was below C/100. The results were plotted in a manner resembling cyclic voltammograms except that the current is replaced by specific capacity. The result shows only one sharp peak while the system is desodiated. In the charge process, there is an oxidation peak at 0.94V, while in the discharge process the corresponding reduction peak is at 0.92V. The hysteresis between charge and discharge is quite small. These peaks indicate reversible phase transition at about 0.93V, which is in good agreement with the results of galvanostatic battery test.

In the first discharge, the peak area in the low voltage region is larger than that of charge process. For the second discharge, the difference of the peak areas in the low voltage region between discharge and charge is obviously decreased. Since peak area in the capacity versus voltage graph is a measurement of specific capacity, this result confirms that there are some irreversible reactions happened in the low voltage region. The irreversible reaction can be ascribed to SEI formation and irreversible sodium insertion in carbon. This provides extra explanation for the capacity loss during the first discharge. The similarity of charge and discharge profile indicates reversible reaction and good cyclability in the following cycles.

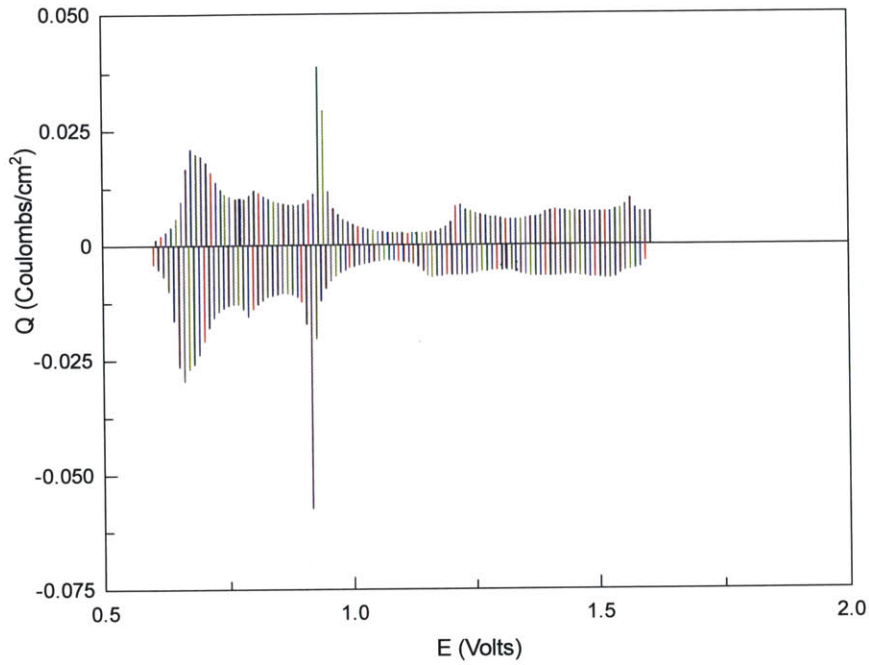

Figure2-18 Capacity vs voltage of Na deintercalation and intercalation for NaTiO2 measured by PITT in the 0.6-1.6V voltage window.

Fig2-19 shows the capacity versus voltage measured by PITT of $NaTiO_2$ in the extended voltage range of 0.6-1.7V. It worth noting that an additional peak occurs at 1.685V, and the corresponding relaxation time of current at this voltage is prolonged. This indicates a irreversible phase transition possibly from two-dimensional layered O3'-type structure to three-dimensional spinel structure caused by Ti migration into the sodium layer. This result provides additional proof for our conclusion of structure modification based on galvanostatic charge and discharge performance with high voltage cutoff.

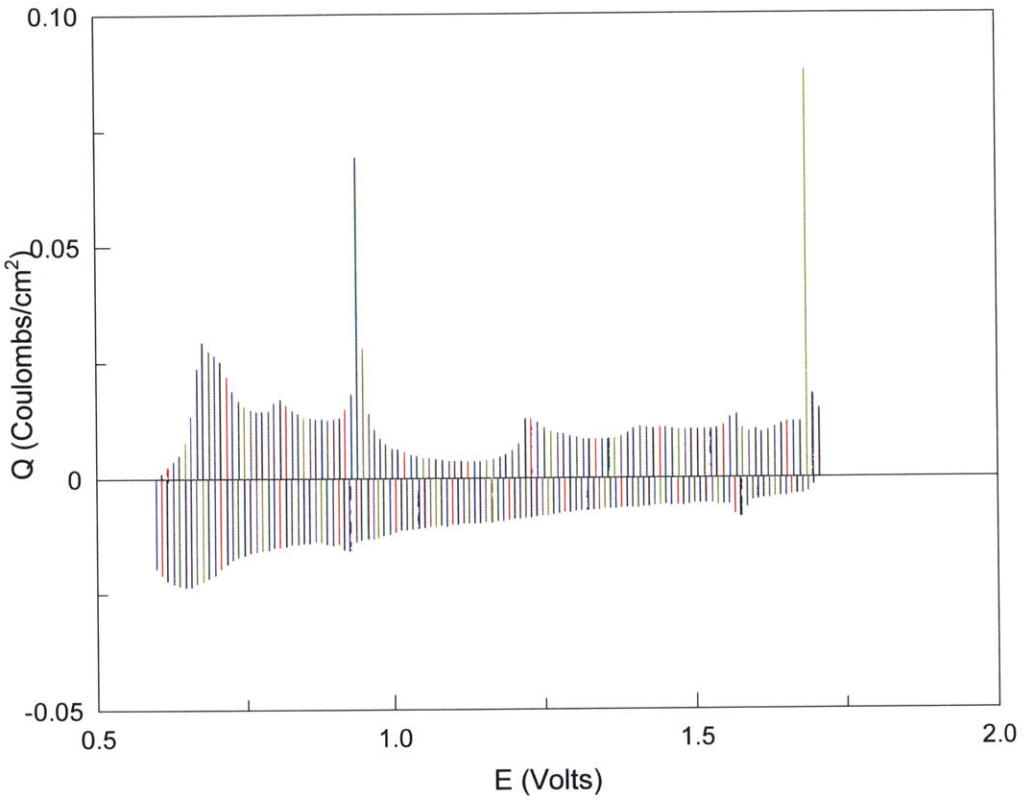

Figure2-19 Capacity vs voltage of Na deintercalation and intercalation for NaTiO2 measured by PITT in the 0.6-1.7V voltage window

3 Understanding of reaction mechanism

3.1 Structure evolution study by *in situ* XRD

To study the electrochemical sodium insertion/extraction mechanism, *in situ* X-ray diffraction experiments were performed during the charge and discharge of a cell that was previously discharged to 0.6V corresponding to the O3-$NaTiO_2$ composition. Fig3-1 shows the X-ray diffraction patterns in the 6.5°-30.5° two-theta range (Kα 1 & Kα 2 of Mo source) of an *in situ* cell continuously charged/discharged at C/20 rate. The phase transitions at 0.93V shown in these patterns clearly are in good agreement with the results obtained from electrochemical data. Note that in the whole two-theta range, preferred orientation exists because the electrode films were prepared by a dry method that involved multiple pressing and rolling process. The preferential orientation enhanced the intensity of (00l) peaks and lowered the intensity of peaks in other directions[16,21,22].

After charged to 0.93V, the diffraction patterns obviously change from those of the O3 phase to O3' phase, indicating a phase transition. And this phase transition is found to be reversible in the discharge process. A detailed analysis will be discussed in the following part.

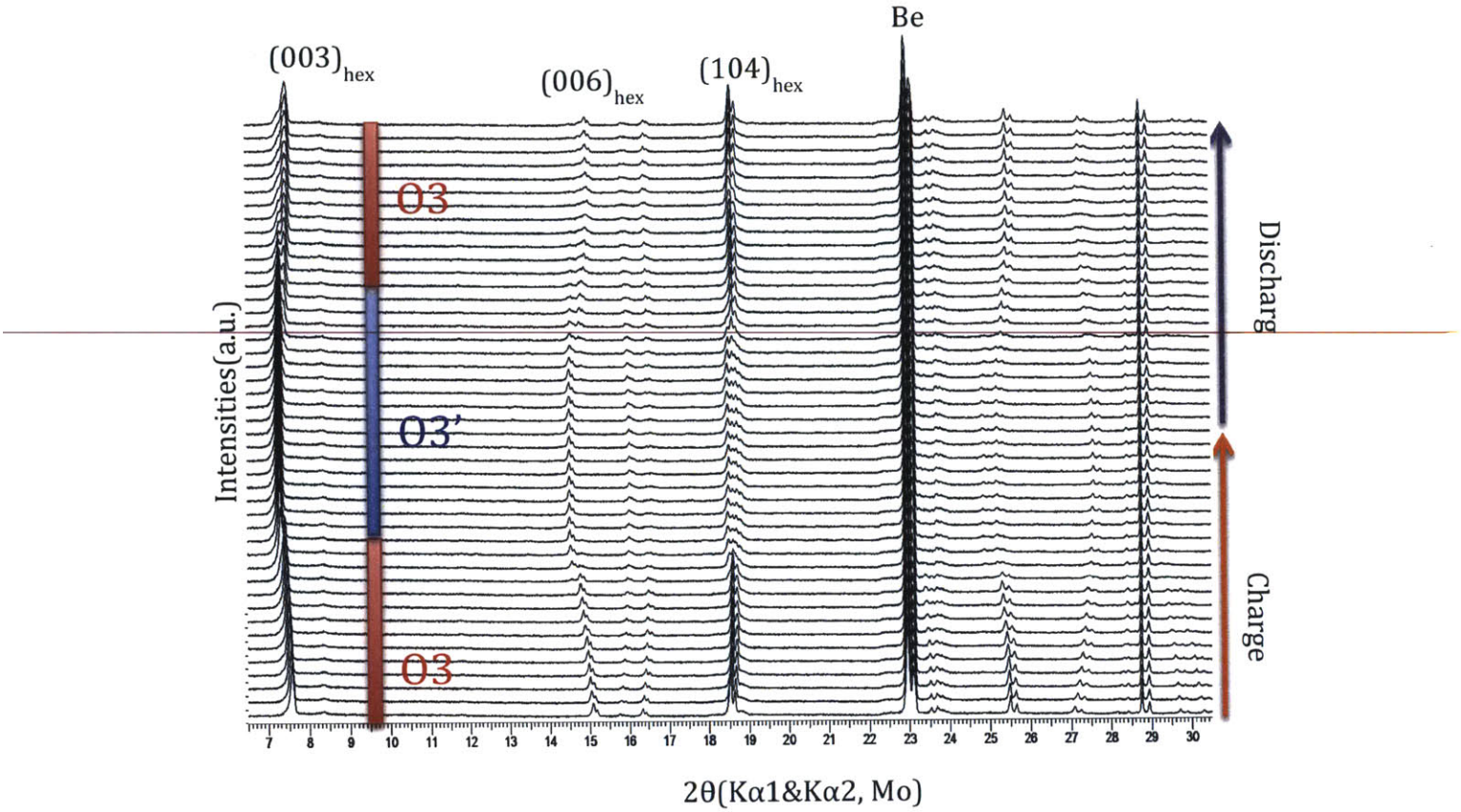

Figure3-1. X-ray diffraction patterns in the 6.5°-30.5° two-theta range (Kα 1 & Kα 2 of Mo source) of an *in situ* cell continuously charged/discharged at C/20 rate

In the charge range of 0.6-0.93V, Na_xTiO_2 remains O3-type structure with a hexagonal system. As shown in Fig3-2, the c_{hex} parameter is equal to three times of the interslab distance (interplanar spacing of (003)) in the hexagonal cell, and a_{hex} is an average of in-plane Ti-Ti distances[11]. Lattice parameters are very sensitive to the sodium content[16,20,21]. During sodium deintercalation in the charge process, the global evolution trend of the (003) diffraction peak is a shift to lower two-theta angles, shown in Fig3-3. This phenomenon is commonly observed in the layered materials[4,15,16,20,21]. This demonstrates that c_{hex} parameter increases owing to the

loss of cohesiveness when sodium ions are extracted from the interslab space. In parallel, the a_{hex} parameter, which is equal to the Ti-Ti distance within the slabs, decreases owing to the oxidation of titanium[11,21]. As other A_xMO_2 (A=Na, Li, M=transition metal) layered materials, the cell parameters change continuously in the solid solution domain of O3 phase.

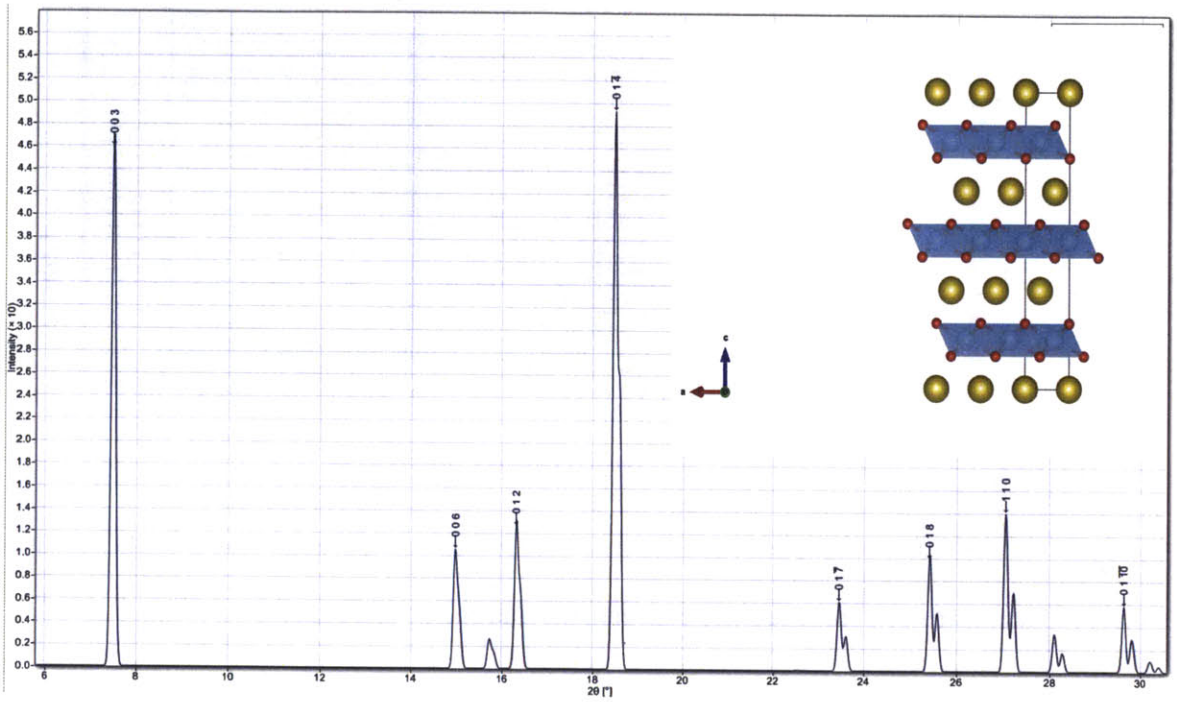

Figure3-2. Schematic illustration of O3 structure and simulated XRD pattern

The variations of theses cell parameters in O3 phase calculated from *in situ* X-ray diffraction patterns are presented as a function of sodium content in Fig3-4. The c_{hex} parameter evolution can also be presented by the variation of the position of (006) peaks, which gives half of the changes in the interslab distance.

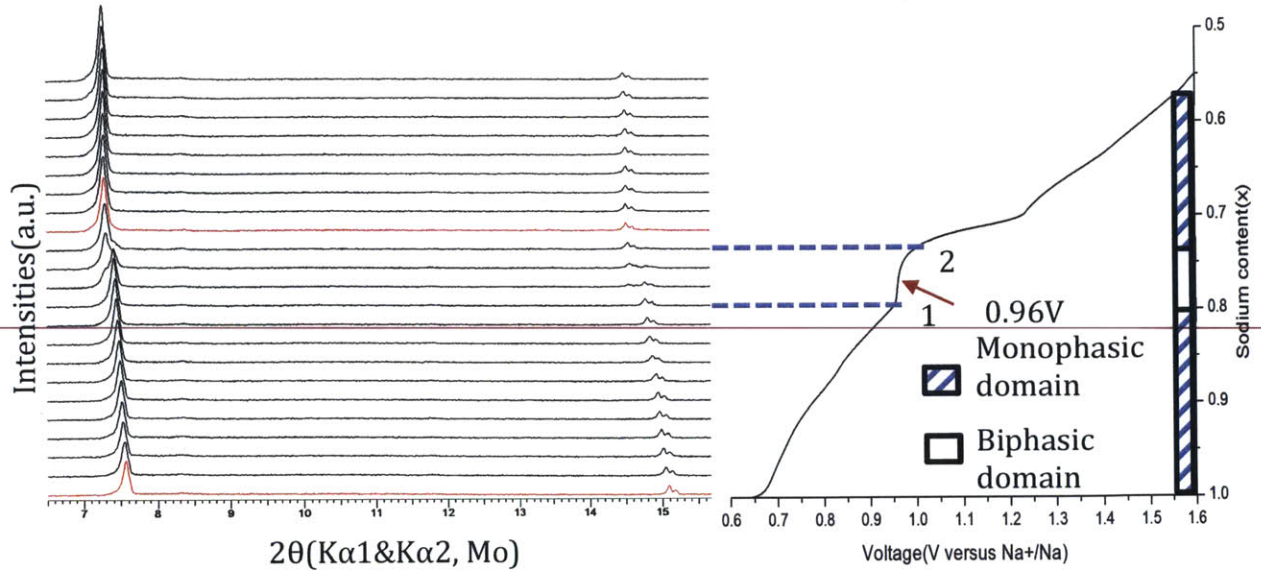

Figure3-3 Evolution of $(003)_{hex}$ peak and $(006)_{hex}$ from *in situ* XRD during galvanostatic charge at C/20.

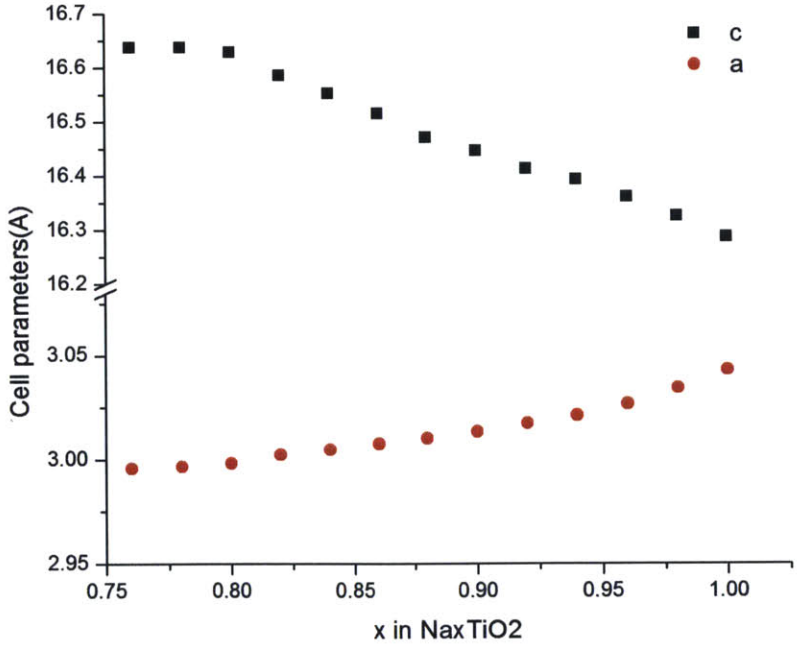

Figure3-4 Lattice parameters a_{hex} and c_{hex} of O3 phase calculated from *in situ* XRD upon charge

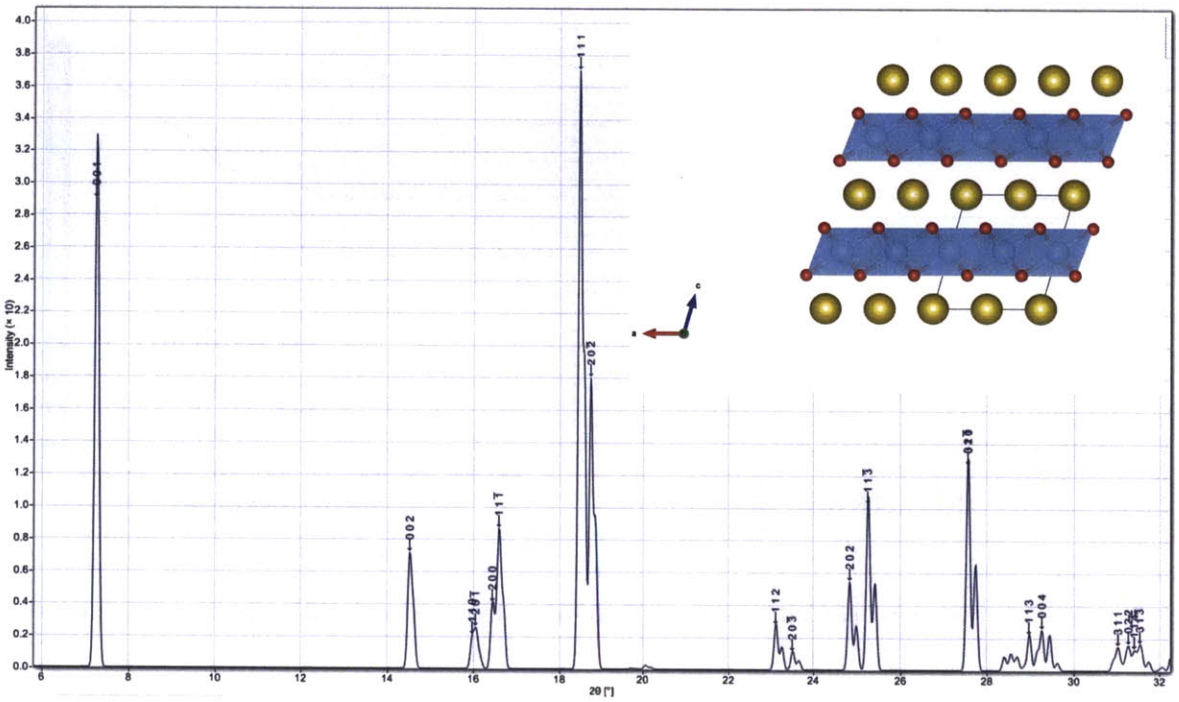

Figure3-5 Schematic illustration of O3' structure and simulated XRD pattern.

When the cell is charged up to the voltage plateau at 0.93V, a new peak arises at a lower angle compared with the $(003)_{hex}$ diffraction peak, and the $(104)_{hex}$ diffraction peak splits into two peaks, which indicates a two-phase domain corresponding to a phase transition. In the biphasic domain, the splitting of peaks is caused by monoclinic distortion of the crystal structure.

In the biphasic regions of layered materials, usually the cell parameters remain constant[11,16,20,21]. Nevertheless, in the O3' Na_xTiO_2 case, the cell parameters of the new-formed phase vary slightly during sodium deintercalation. Similar results have been observed in P2-type $NaVO_2$[21]. Because the plateau at 0.93V is short, which means the biphasic domain of O3 and O3' forms in a narrow sodium content, and preferred orientation lowered the intensity of (hk0) peaks, it's difficult to get

precise information on the evolution of a_{hex} parameter. In addition, since the X-ray source is Mo Kα1 and Kα2, we encountered difficulties in clearly identifying whether the two close diffraction peaks were due to a biphasic domain or the non-monochromatic wavelength. As a consequence, the behavior of lattice parameter variation in the bi-phasic domain may result from the data quality or the in homogeneity of the new-formed phase during continuous charging process that doesn't reach equilibrium completely.

With an increasing charge depth, more sodium ions are extracted from the interslabs, accompanied by structural distortion from hexagonal structure to monoclinic structure, corresponding to O3 phase and O3' phase respectively (See Fig3-5). This is demonstrated by the peak shifting and splitting behaviors *in situ* XRD patterns in the voltage range of 0.93V-1.57V.

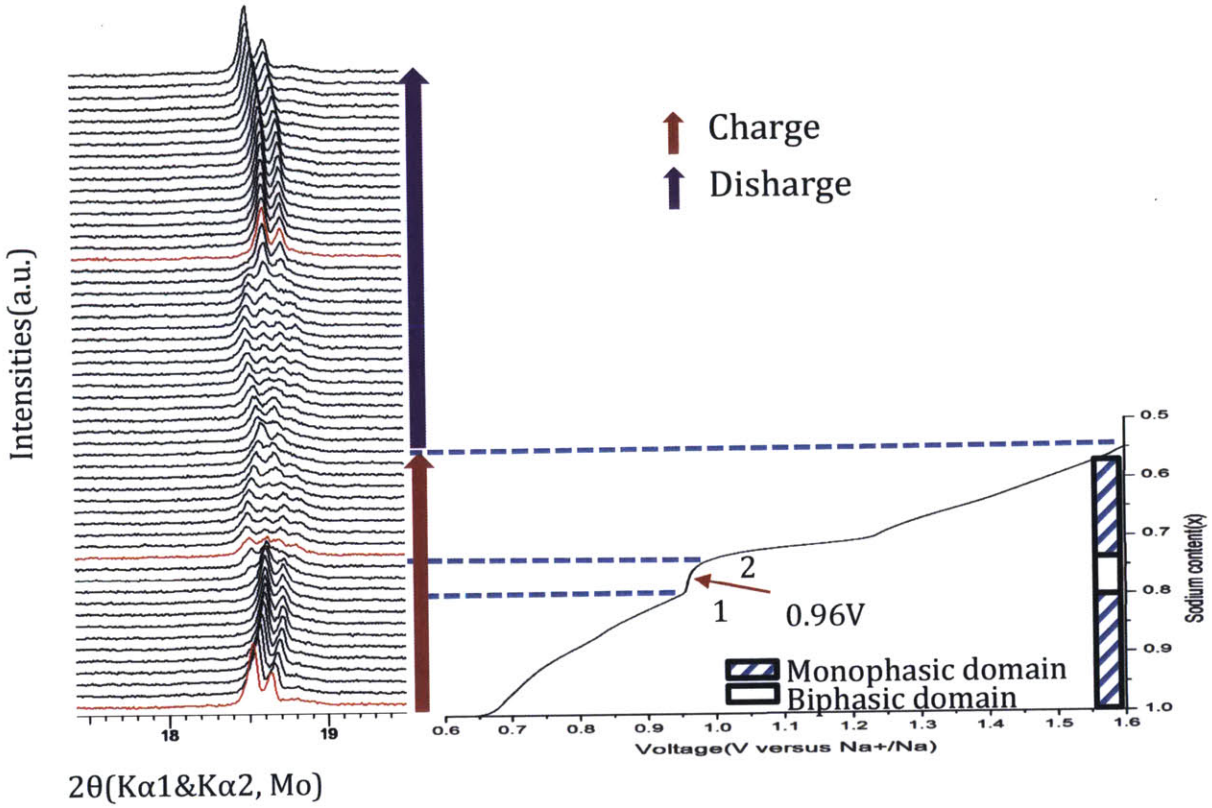

Figure3-6 Evolution of $(104)_{hex}$ peak from *in situ* XRD during galvanostatic charge and discharge at C/20 rate.

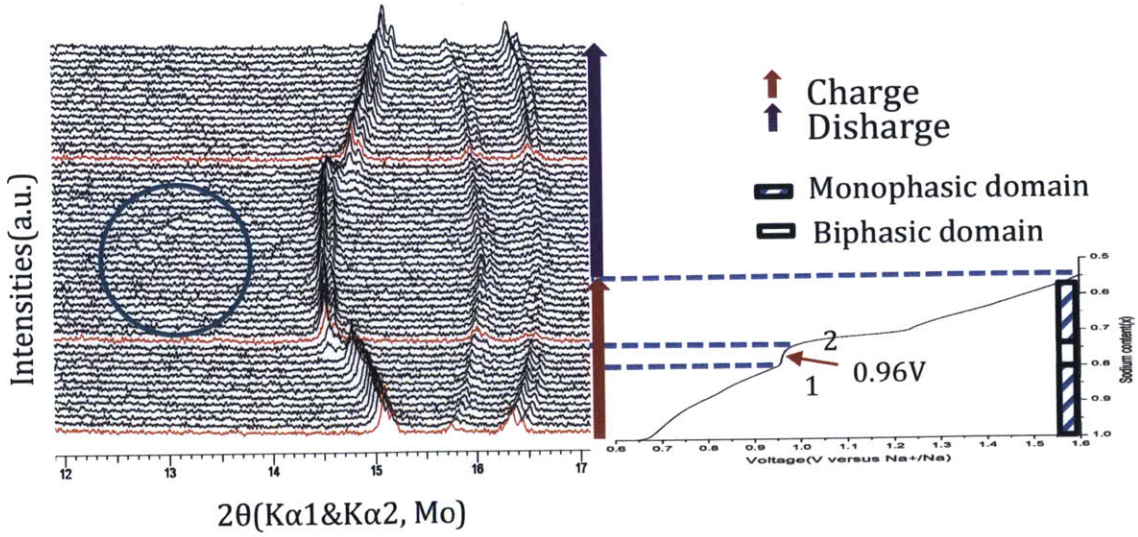

Figure3-7 Evolution of peaks in the 12°-17° two-theta range from *in situ* XRD during during galvanostatic charge and discharge at C/20 rate.

As shown in Fig3-5, O3' phase remains a layered structure, whereas beta angle is around 110° rather than 90° in O3 phase, displaying a monoclinic distortion. Therefore, the interslab distance (interplanar distance of (001)) is equal to $c_{mon}*\sin\beta_{mon}$, while the average intraslab distances are $a_{mon}*\sin\beta_{mon}$ and b_{mon} corresponding to interplanar distance of (100) and (010) respectively.

An appealing point is that $(001)_{mon}$ and $(002)_{mon}$ peaks keeps in the same two-theta position during charge after slightly shifting to lower angle at the end of bi-phasic domain, indicating the interslab distance remains constant during continuous desodiation. This phenomenon is completely opposite to the lattice parameter evolution of other layered materials during sodium deintercalation[14-22]. Commonly, in the single-phasic domain, the interslab distance increases due to the loss of cohesiveness when Na^+ ions are extracted from the interslab space, while in the biphasic domain, the interslab distance remains constant, just as the c parameter variation of O3 Na_xTiO_2 phase discussed above. Meanwhile, $(111)_{mon}$ and $(20\text{-}2)_{mon}$ peaks shifts to higher two-theta angle, indicating that the in-plane distance corresponding to the Ti-Ti distance within the slabs is continuously varying upon desodiation.

To improve the precision of calculating the lattice parameters during sodium deinterclation, *In situ* X-ray diffraction data of higher quality are obtained while the in *in situ* cell is charged potentiostatically. The in situ cell is potentiostatically hold for 4 hours at each voltage step to reach the equilibrium state. In parallel, each XRD scan lasts 4 hours to simultaneously record the information of structural evolution.

The variation of intersheet and intrasheet distance versus sodium content of O3' single-phase domain is shown in Fig3-8, 9. In addition, the variations of a_{mon}, b_{mon}, c_{mon} and β_{mon} of O3' phase upon charging versus sodium content are shown in Fig3-10, respectively, to illustrate the detailed lattice parameters evolution trend.

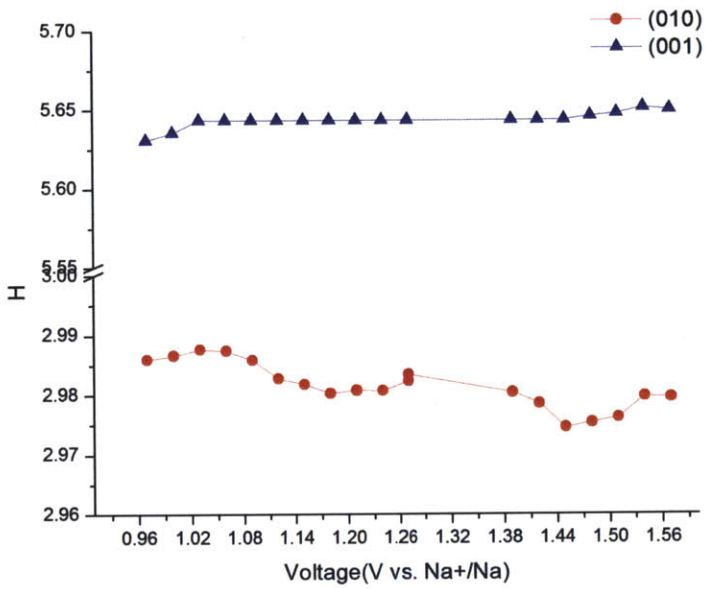

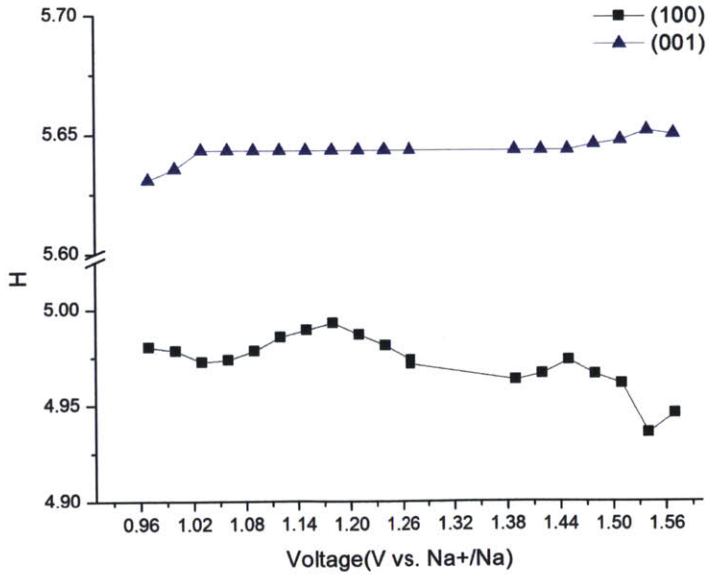

Figure3-9 (a) Variation of intersheet $(001)_{mon}$ and intrasheet $(010)_{mon}$ distance versus sodium content of O3' phase; (b) Variation of intersheet $(001)_{mon}$ and intrasheet $(100)_{mon}$ distance versus sodium content of O3' phase from *in situ* XRD during charge.

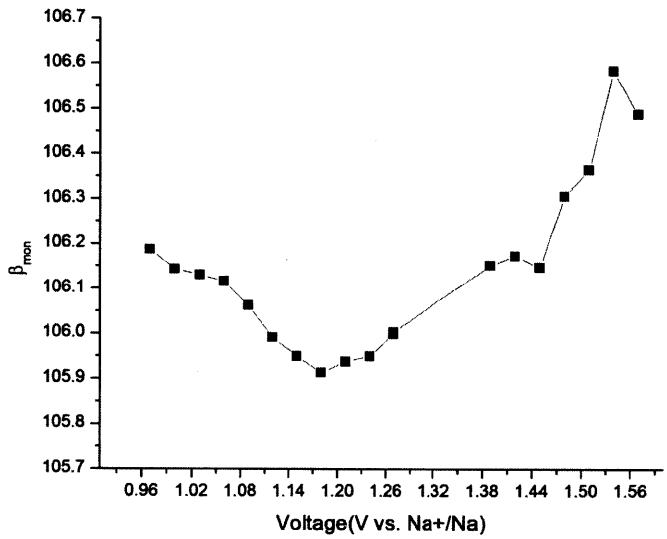

Figure3-10 Variation of a_{mon}, b_{mon}, c_{mon} and β_{mon} versus sodium content of O3' phase from *in situ* XRD during charge.

It's worth noting that the X-ray diffraction patterns during the sodium deintercalation clearly show the presence of additional weak Bragg peaks characteristic of superstructures. The present additional Bragg peaks in the 12°-14° and 17°-18° two-theta range (Fig3-7, Fig3-11) are not indexed in the basic O3'-type structure. The strongest superstructure peak is the one in the 12°-14° two-theta range that appears at around 13.5° and remains at the same angle until the battery is charged up to the inflection point of the voltage curve. After the inflection point (corresponding to 1.2V of *in situ* cell or ~$Na_{0.77}TiO_2$; in the Swagelok cell, the voltage

of inflection point is 1.18V due to a smaller polarization compared with *in situ* cell), this peak starts to shift to a lower angle during the desodiation process. A similar behavior is also observed for the additional peak at around 17.9°. These superstructure peaks exhibit a very significant shift—the extent of shifting is much more pronounced than the basic peaks of O3' phase. This fact suggests the existence of a structural modulation with a modulation vector varying as a function of the sodium content[11,16,20,21].

Another interesting behavior is observed when the *in situ* cell is charged up to the weak inflection point on the voltage curve (corresponding to 1.45V or $Na_{0.6}TiO_2$). Superstructure peaks at around 13° gradually disappear while some new additional weak Bragg peaks show up at 14.4°. And the generated superstructure peak significantly shifts to lower angle following a similar behavior of the superstructure peaks in the 13°-14° two-theta range. This indicates a further structural modulation occurs with increasing charge depth.

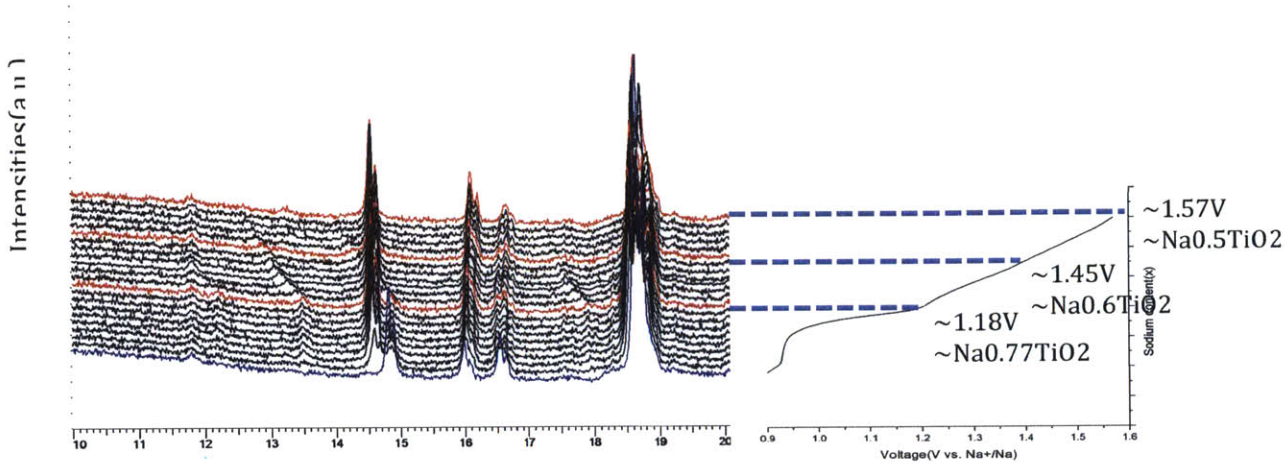

Figure3-11 *In situ* XRD data in the 10°-20° two-theta range recorded during the PITT experiments.

After the *in situ* cell is charged up to the third inflection point on the voltage curve (corresponding to 1.57V or $Na_{0.5}TiO_2$), the weak additional peaks disappear. Meanwhile, the distance between $(111)_{mon}$ and $(20\text{-}2)_{mon}$ peaks gets smaller obviously with a trend of merging(See Fig3-12).

The formation of these superstructures seems to result from Na/vacancy ordering that lowers the symmetry. The variation trend of lattice parameter of O3' phase can be associated with structure modulations, as shown in Fig3-13.

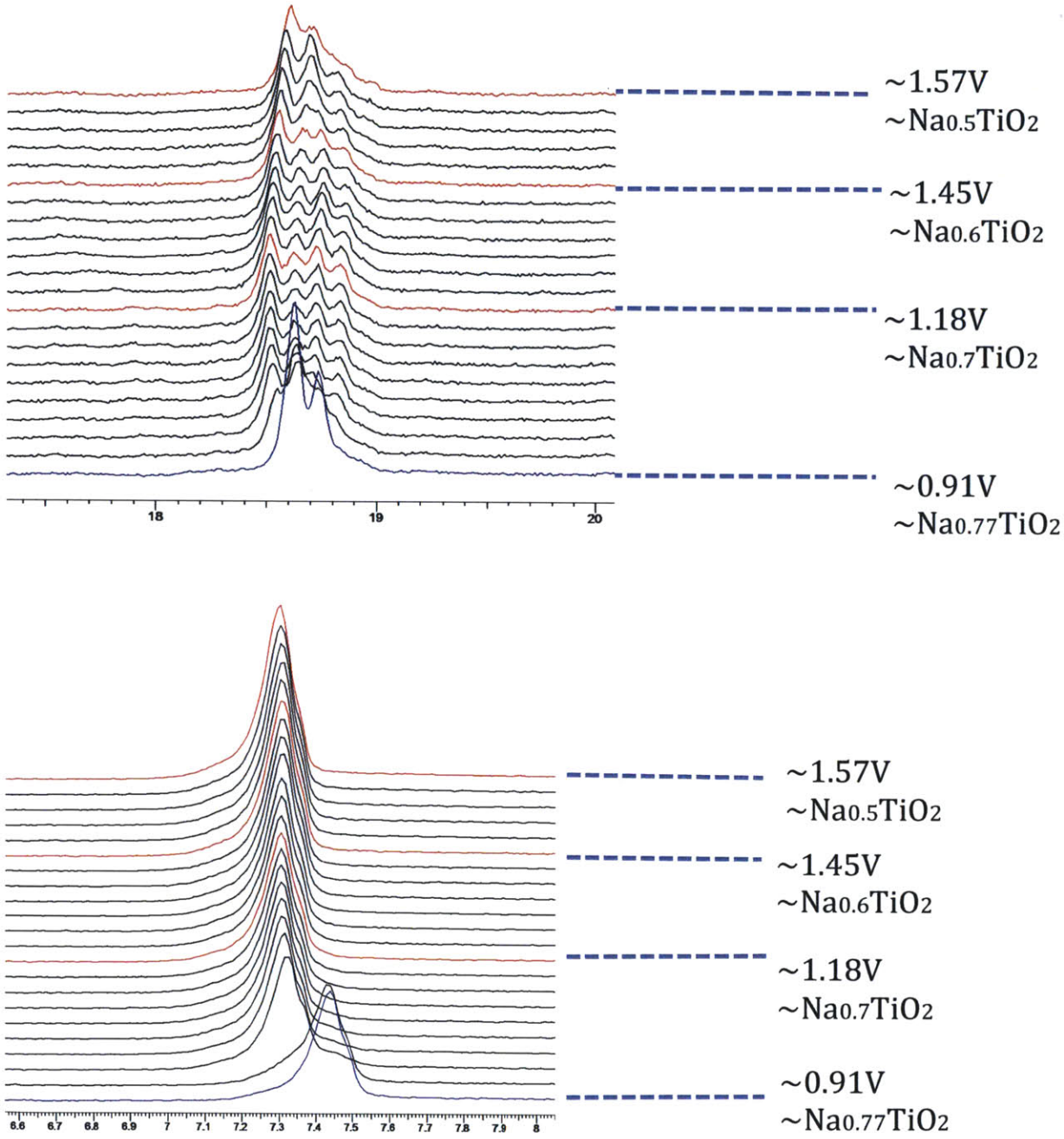

Figure3-12 (a) Evolution of $(001)_{mon}$ peak from *in situ* XRD during PITT test; (b) Evolution of $(111)_{mon}$ and $(20\text{-}2)_{mon}$ peaks from *in situ* XRD during PITT test.

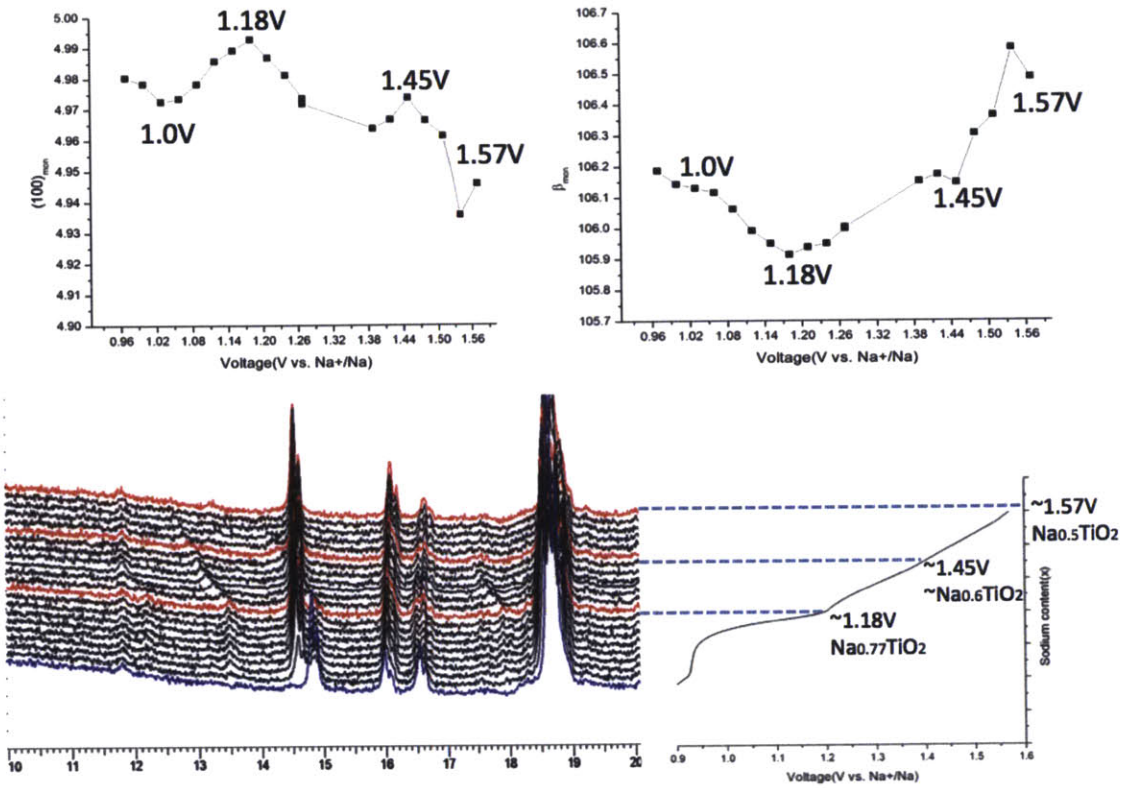

Figure3-13 Synergy between lattice parameter variation and superstructure evolution

To give a general overview of the lattice parameter evolution during sodium deintercalaction, all X-ray diffraction patterns were indexed in the hexagonal system. Therefore, for O3' phase with monoclinic distortion, $a_{mon}/\sqrt{3}$ represents the average in-plane Ti-Ti distance compared with the hexagonal cell, and c_{hex} parameter remains the same. The overall evolution of lattice parameters as a function of sodium content is shown in Fig3-14.

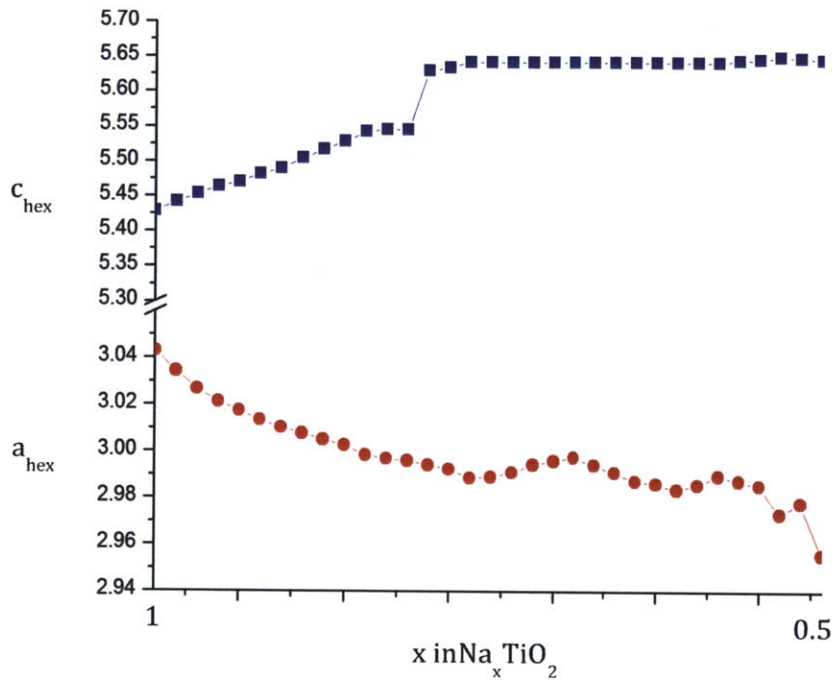

Figure3-14 Overall evolution of the lattice parameters a_{hex} and c_{hex} calculated from *in situ* XRD during charge.

3.2 Irreversible structure modification upon overcharge

As discussed in Chapter 2, if the battery is charged above 1.57V, corresponding to over 0.5 Na extracted per formula unit, irreversible structure modification happens. As shown in Fig2-7, the cell polarization is considerably higher by comparing the charge and discharge voltage curves. The cell resistance increases strongly as over 0.5 Na is deintercalated, which is confirmed by the gradually increase of current during relaxation in PITT test. Cell capacity decays quickly during cycling in the 0.6-

2.0V voltage window, owing to continuously accumulated structure modification at the high voltage region with cycling.

To directly illustrate the structure modification, *in situ* X-ray diffraction is performed as the cell is charged above 1.57V, correspond to more than 0.5 Na is deintercalated. During the deintercalation, a biphasic region is observed at about 1.6V, which indicates a first-order phase transition. The X-ray diffraction pattern of the new phase can be indexed with a rhombohedral system.

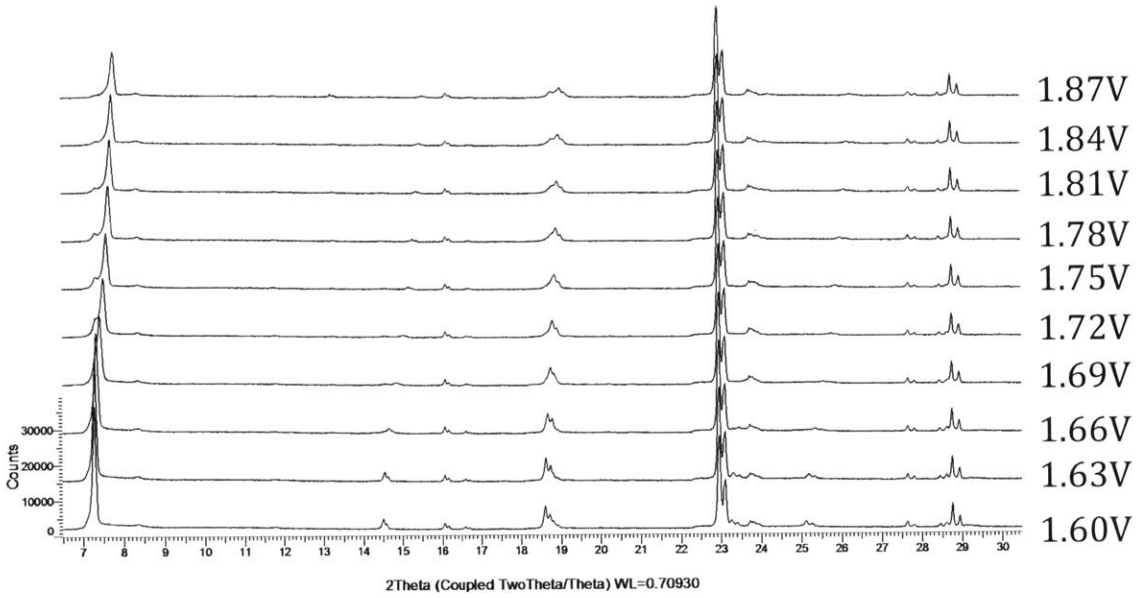

Figure 3-15 *In situ* XRD patterns during charge from 1.6V up to 1.87V.

The structure evolution during desodiation above 1.6V is shown in Fig3-15. $(003)_{hex}$ peak shifts to a higher two-theta angle, indicating that the interslab distance decreases rapidly upon charging over 1.6V, corresponding to over 0.5 Na is extracted. Previous discussion has explained that the interslab distance increases during deintercaltion in A_xMO_2 materials of layered structures. The observed decrease of interslab distance indicates a modification of cationic distribution. A

possible explanation is Na_xTiO_2 layered structure become unstable when the sodium content is getting smaller. To stabilize the structure, some tetravalent titanium ions migrate from the transition metal layer to the interslab sodium plane. The presence of highly-charged Ti^{4+} ions in the sodium layer leads to a strong contraction of the interslab distance. So the c_{hex} parameter is considerably decreased. With continuously Ti^{4+} migration during charge, the level of cations mixing in the intersheet layer is enhanced. Therefor, this material should be considered as a three-dimensional structure, rather than a two-dimensional layered one.

During the discharge from the modified phase, even at very slow rate of C/100, the O3 and O3' layered phases do not reappear. Sodium ions intercalate into the available sites in the sodium layer without modification of the 3D framework. The capacity of discharge depends on the amount of migrated Ti^{4+} in the sodium layer. The 2D→3D phase transition is irreversible, which possibly due to the absence of no driving force that could force titanium ions migrate back to their original layer during discharge. Calculation by S. Kim[28] shows that stability of the spinel type structure is actually higher than that of O3-type layered structure at x=0.5 in Na_xTiO_2. Based on experimental and computational results, it's reasonable to assume that the irreversible structure modification at low Na content is caused by migration of Ti^{4+}. More detailed investigation to explain this behavior is in progress.

3. Conclusions

In summary, O3-$NaTiO_2$ is synthesized and tested electrochemically as a negative electrode material for sodium-ion batteries. About 0.5 Na can be reversibly intercalated/deintercalated in $NaTiO_2$, corresponding to a reversible capacity of 130mAhg^{-1}. To achieve high capacity and best cyclability, the effect of voltage range on the electrochemical performance of $NaTiO_2$ is studied. 0.6-1.6V is found to be the optimal voltage window for galvanostatic cycling. In addition, sodium insertion/extraction mechanism is investigated by in situ X-ray diffraction. A reversible O3 to O3' phase transition is observed at 0.93V. Special Na/vacancy orderings occurs during sodium deintercalation, which leads to an unusual lattice parameter variation. The interslab distance of O3' phase remains constant during charge, while the in-plane distance keeps varying.

With high capacity and excellent cyclability, O3-$NaTiO_2$ is among the best available anode materials for sodium ion batteries. By combining O3-$NaTiO_2$ with appropriate cathode materials, it could be possible to assemble high energy density sodium ion batteries that only consist of earth abundant elements. We believe that these findings enrich the exploration of promising anode materials for rechargeable sodium-ion batteries for large-scale energy storage applications.

References

1. Dunn, B., Kamath, H. & Tarascon, J.-M. Electrical energy storage for the grid: a battery of choices. *Science* **334,** 928–35 (2011).

2. Pan, H., Hu, Y.-S. & Chen, L. Room-temperature stationary sodium-ion batteries for large-scale electric energy storage. *Energy Environ. Sci.* **6,** 2338 (2013).

3. Kim, S.-W., Seo, D.-H., Ma, X., Ceder, G. & Kang, K. Electrode Materials for Rechargeable Sodium-Ion Batteries: Potential Alternatives to Current Lithium-Ion Batteries. *Adv. Energy Mater.* **2,** 710–721 (2012).

4. Wang, Y. *et al.* A zero-strain layered metal oxide as the negative electrode for long-life sodium-ion batteries. *Nat. Commun.* **4,** 2365 (2013).

5. Ge, P. & Fouletier, M. Electrochemical Intercalation of Sodium in Graphite.*Solid State Ionics,* **30,** 1172–1175 (1988).

6. Komaba, S. *et al.* Electrochemical Na Insertion and Solid Electrolyte Interphase for Hard-Carbon Electrodes and Application to Na-Ion Batteries. *Adv. Funct. Mater.* **21,** 3859–3867 (2011).

7. Sun, Y. *et al.* Direct atomic-scale confirmation of three-phase storage mechanism in Li4Ti5O12 anodes for room-temperature sodium-ion batteries. *Nat. Commun.* **4,** 1870 (2013).

8. Zhu, H. *et al.* Tin Anode for Sodium-Ion Batteries Using Natural Wood Fiber as a Mechanical Buffer and Electrolyte Reservoir. *Nano Lett.* **13**,3093-3100 (2013).

9. Darwiche, A. *et al.* Better cycling performances of bulk Sb in Na-ion batteries compared to Li-ion systems: an unexpected electrochemical mechanism. *J. Am. Chem. Soc.* **134,** 20805–11 (2012).

10. Shilov, G. , Nalbandyan, V. , Volochaev, V. & Atovmyan, L. Crystal growth and crystal structures of the layered ionic conductors–sodium lithium titanium oxides. *Int. J. Inorg. Mater.* **2,** 443–449 (2000).

11. Mazzaz.A. et al. A Study of the Na_xTiO_2 System by Electrochemical Deintercalation. *Journal of Inclusion Phenomena,* 45–51 (1983).

12. Delmas. C. et al. Structural Classification and Properties of the Layered Oxides. *Physica* 99B, 81-85(1980)

13. Delmas. C. et al. Electrochemical Intercalation of Sodium in NaxCoO2 Bronzes, *Sol. State* Ionics, 3/4, 165–169 (1981).

14. Hagenmuller, P. Sur de Nouveaux Bronzes Oxygenes de Formule NaxCoO2 (x<l). Le Systeme Cobalt-Oxygene-Sodium. **537,** 532–537 (1973).

15. Komaba, S., Takei, C., Nakayama, T., Ogata, A. & Yabuuchi, N. Electrochemical intercalation activity of layered NaCrO2 vs. LiCrO2. *Electrochem. commun.* **12,** 355–358 (2010).

16. Berthelot, R., Carlier, D. & Delmas, C. Electrochemical investigation of the P2–NaxCoO2 phase diagram. *Nat. Mater.* **10,** 74–80 (2011).

17. Ma, X., Chen, H. & Ceder, G. Electrochemical Properties of Monoclinic NaMnO2. *J. Electrochem. Soc.* **158,** A1307 (2011).

18. Vassilaras, P., Ma, X., Li, X. & Ceder, G. Electrochemical Properties of Monoclinic NaNiO2. *J. Electrochem. Soc.* **160,** A207–A211 (2012).

19. M. Sathiya, K. Hemalatha, K. Ramesha, J.-M. Tarascon, and A. S. Prakash, Synthesis, Structure, and Electrochemical Properties of the layered Sodium Insertion Cathode Material:$NaNi_{1/3}Mn_{1/3}Co_{1/3}O_2$, *Chem. Mater.* **24**. 1846-1853.(2012).

20. Yoshida, H., Yabuuchi, N. & Komaba, S. $NaFe_{0.5}Co_{0.5}O_2$ as high energy and power positive electrode for Na-ion batteries. *Electrochem. commun.* **34,** 60–63 (2013).

21. Guignard, M. *et al.* P2-$Na_{(x)}VO_2$ system as electrodes for batteries and electron-correlated materials. *Nat. Mater.* **12,** 74–80 (2013).

22. Guignard, M. *et al.* Vanadium Clustering / Declustering in P2–$Na_{1/2}VO_2$ Layered Oxide. *Chem. Mater.* **26**,1538-1548 (2014).

23. Komaba, S. *et al.* Study on the Reversible Electrode Reaction of Na1-xNi0.5Mn0.5O2 for a Rechargeable Sodium-Ion Battery,*Inorg. Chem.* **51**,6211-6220 (2012).

24. Mortemard de Boisse, B., Carlier, D., Guignard, M. & Delmas, C. Structural and Electrochemical Characterizations of P2 and New O3-$Na_xMn_{1-y}Fe_yO_2$ Phases Prepared by Auto-Combustion Synthesis for Na-Ion Batteries. *J. Electrochem. Soc.* **160,** A569–A574 (2013).

25. Clarke, S. J., Fowkes, A. J., Harrison, A., Ibberson, R. M. & Rosseinsky, M. J. Synthesis , Structure, and Magnetic Properties of $NaTiO_2$. **4756,** 372–384 (1998).

26. Brummer, B. The Effect of Desiccants on the Cycling Efficiency of the Lithium Electrode in Propylene Carbonate-based electrolytes. *Electrochemcia Acta*, **23**, 55-62(1978).

27. Huang, J. P. *et al.* Electrochemical sodium storage of TiO_2(B) nanotubes for sodium ion batteries. *RSC Adv.* **3,** 12593 (2013).

28. Kim, S., Ma, X., Ong, S. P. & Ceder, G. A comparison of destabilization mechanisms of the layered $Na_{(x)}MO_2$ and $Li_{(x)}MO_2$ compounds upon alkali de-intercalation. *Phys. Chem. Chem. Phys.* **14,** 15571–8 (2012).